Permeability During Magma Expansion and Compaction

Helge. M. Gonnermann[1], Thomas Giachetti[2] (ID), Céline Fliedner[1], Chinh T. Nguyen[1], Bruce F. Houghton[3] (ID), Joshua A. Crozier[2] (ID), and Rebecca J. Carey[4]

[1]Department of Earth Environmental and Planetary Sciences, Rice University, Houston, TX, USA, [2]Department of Earth Sciences, University of Oregon, Eugene, OR, USA, [3]Department of Geology and Geophysics, University of Hawai'i at Mānoa, Honolulu, HI, USA, [4]School of Earth Sciences, University of Tasmania, Hobart, Tasmania, Australia

Abstract Plinian lapilli from the 1060 Common Era Glass Mountain rhyolitic eruption of Medicine Lake Volcano, California, were collected and analyzed for vesicularity and permeability. A subset of the samples were deformed at a temperature of 975°, under shear and normal stress, and postdeformation porosities and permeabilities were measured. Almost all undeformed samples fall within a narrow range of vesicularity (0.7–0.9), encompassing permeabilities between approximately 10^{-15} m² and 10^{-10} m². A percolation threshold of approximately 0.7 is required to fit the data by a power law, whereas a percolation threshold of approximately 0.5 is estimated by fitting connected and total vesicularity using percolation modeling. The Glass Mountain samples completely overlap with a range of explosively erupted silicic samples, and it remains unclear whether the erupting magmas became permeable at porosities of approximately 0.7 or at lower values. Sample deformation resulted in compaction and vesicle connectivity either increased or decreased. At small strains permeability of some samples increased, but at higher strains permeability decreased. Samples remain permeable down to vesicularities of less than 0.2, consistent with a potential hysteresis in permeability-porosity between expansion (vesiculation) and compaction (outgassing). We attribute this to retention of vesicle interconnectivity, albeit at reduced vesicle size, as well as bubble coalescence during shear deformation. We provide an equation that approximates the change in permeability during compaction. Based on a comparison with data from effusively erupted silicic samples, we propose that this equation can be used to model the change in permeability during compaction of effusively erupting magmas.

1. Introduction

Single eruptions of silica-rich magmas frequently encompass phases of intense explosive as well as effusive activity (e.g., Adams, Houghton, Fagents, & Hildreth, 2006; Castro et al., 2013; Donnelly-Nolan et al., 2008; Gardner et al., 1998; Lara, 2009; Nairn et al., 2004; Saubin et al., 2016; Schipper et al., 2013). Despite variability in detail, the majority of pyroclasts from high-intensity explosive phases have porosities of approximately 0.7–0.8 (e.g., Houghton & Wilson, 1989; Mueller et al., 2011), corresponding to a vesicle-to-matrix ratio of approximately 2 to 4. Because the concentrations of magmatic water within the matrix glass of pyroclasts record near-atmospheric pressures (Giachetti & Gonnermann, 2013; Giachetti et al., 2015; Seligman et al., 2016), it stands to reason that the magma decompressed to approximately atmospheric pressure before quenching. Given typical estimates of pre-eruptive dissolved volatiles (e.g., Wallace, 2005), magma decompression to atmospheric pressure as a closed system, which is without loss or gain in volatiles, is expected to result at equilibrium in gas-to-melt volume ratios that are about 100-fold higher than typically observed in pyroclasts (Cashman & Mangan, 1994; Thomas et al., 1994). Porosities of effusively erupting magmas are even lower, down to zero in the case of obsidian, despite similar amounts of pre-eruptive dissolved volatiles in effusively and explosively erupted magmas (e.g., Eichelberger et al., 1986; Newman et al., 1988). The discrepancy between theoretical closed-system and observed porosities is thought to be the consequence of open-system degassing, with a net loss of volatiles from the magma (Eichelberger et al., 1986; Westrich & Eichelberger, 1994), presumably following a period of vesiculation and increasing porosity. This is a consequence of the net loss of pore fluid from the magma by permeable flow, together with viscous flow of the surrounding silicate melt, referred to as "compaction" (McKenzie, 1984).

We will use the term "gas" to refer to exsolved magmatic volatiles, which constitute a supercritical fluid under magmatic conditions. Volatile solubility decreases during eruptive magma ascent, resulting in magma expansion, which encompasses nucleation, growth, and coalescence of volatile-bearing bubbles (e.g., Cashman & Mangan, 1994; Sparks, 1978; Sparks et al., 1994). We will refer to the combination of these processes as magma "vesiculation." The volume fraction of magma occupied by exsolved volatiles will interchangeably be referred to as "vesicularity" or "porosity" (Cashman & Scheu, 2015). It should be noted, however, that porosity is more general and refers to any void space, including fractures. Although the words "vesicle" and "bubble" may also be used interchangeably, our usage will reflect the rationale that bubbles become vesicles when magma quenches (Cashman & Scheu, 2015).

Magma degassing generally refers to the process of volatile exsolution from melt into bubbles. If bubbles do not move relative to the melt that surrounds them, and if volatiles only enter or exit bubbles by diffusion from the melt, the degassing is considered to be a closed-system process. Here the "system" is defined as the given volume of magma. Open-system degassing, in contrast, refers to the case where gas can enter and/or leave a given volume of magma. "Outgassing" (e.g., Cashman & Scheu, 2015; Nimiki & Manga, 2008) is a special case of open-system degassing and refers to the case where the mass of gas exiting the system is greater than that entering it. For silicic magmas, where viscosity is large and buoyant rise of bubbles negligible, outgassing requires that magma is permeable and gas can flow through the magma from high to low gas pressure, along gradients that are likely directed upward and perhaps also radially outward toward conduit walls. Because magma decompresses during ascent, causing exsolved volatiles to expand, outgassing may simply lead to a slower rate of magma expansion and the eruption of magma with lower porosity than under closed-system conditions. If, however, the rate of outgassing is sufficiently high, magma may undergo compaction. The resultant pore geometry represents bubbles that have shrunk in size and no longer have rounded shapes (Westrich & Eichelberger, 1994), referred to as "mature" vesicle texture (e.g., Adams, Houghton, & Hildreth, 2006) and distinct from vesicles textures observed in samples that are not thought to have compacted.

It is believed that outgassing facilitates the nonexplosive eruption of magma (Eichelberger et al., 1986). For example, erupting magma may outgas into conduit walls, if the wall rock is permeable and at given depth contains pore fluid at lower pressure than the magma (Jaupart & Allègre, 1991; Stasiuk et al., 1996). This is expected to be the case for near hydrostatic pore fluid pressure within the wall rock. The time available for permeable gas flow is inversely proportional to magma ascent rate, whereas outgassing into conduit walls is rate limited by permeability. The rate-limiting permeability may either be of the wall rock or of the magma itself. In case of a constant, rate-limiting wall rock permeability, the transition from explosive to effusive activity has been predicted to be a consequence of decreasing ascent rate, all else being equal (Jaupart & Allègre, 1991; Woods & Koyaguchi, 1994).

Permeability within the conduit wall remains poorly constrained. Values used in numerical models (Jaupart & Allègre, 1991; Woods & Koyaguchi, 1994), as well as inferences based on fracture permeabilities of volcanic materials (e.g., Farquharson et al., 2016, 2017), allow for the possibility that despite the potential for magma undergoing shear fracture near the conduit wall (e.g., Gonnermann & Manga, 2003; Kushnir et al., 2017; Tuffen et al., 2003), the wall rock may on average be more permeable than the bulk of the magma. Therefore, magma permeability may ultimately be rate limiting during outgassing. Because magma permeability depends on porosity, as first shown by Eichelberger et al. (1986) and subsequently in numerous analyses (for example Colombier et al., 2017, provide a recent compilation), it is conceivable that outgassing into conduit walls produces compacted magma of low permeability along conduit walls (e.g., Heap et al., 2017; Polacci & Papale, 2001), thereby hindering outgassing from the interior of the conduit. By the same token, magma pressure decreases upward and vertical gas flow within the ascending magma may also lead to outgassing. Eruption models with upward permeable gas flow have assumed that magma permeability is proportional to some power of porosity, encompassing a wide range of possible porosity-permeability relations (e.g., Burgisser et al., 2017; Degruyter et al., 2012; Konzo & Koyaguchi, 2009a, 2009b; Melnik et al., 2005; Melnik & Sparks, 1999, 2002).

It is assumed that magma is impermeable below some threshold in porosity. Theoretically, a porosity threshold exists because bubbles at low volume fractions are sufficiently distant from one another to prevent pervasive coalescence (Blower, 2001b). In percolation theory the formation of long-range connectivity in random systems exists above the "percolation threshold," because a porous volume is considered impermeable until at least one cluster of interconnected pores spans the entire volume. A "percolating cluster" can only

form after a sufficient fraction of the volume is occupied by pores and the minimum volume fraction of pores at which a percolating cluster first exists is called the percolation threshold (e.g., Stauffer & Aharony, 1994). The porosity threshold of volcanic rocks is thus equivalent to the percolation threshold at which a cluster of coalesced bubbles forms an interconnected pathway throughout the magma.

As bubbles nucleate and grow, the melt separating individual bubbles becomes thinner. Bubbles deform to accommodate the increase volume fraction and also due to shear deformation associated with magma flow. In addition to bubble deformation, stretching of the surrounding melt as well as capillary and gravitational forces contribute to the thinning of melt films. As a consequence, melt films can become sufficiently thin to rupture (e.g., Castro, Burgisser, Schipper, & Mancini, 2012; Eichelberger et al., 1986; Klug & Cashman, 1994, 1996; Klug et al., 2002; Nguyen et al., 2013; Proussevitch et al., 1993; Taylor et al., 1983; Toramaru, 1988; Westrich & Eichelberger, 1994). The resultant holes connect adjacent bubbles but grow slowly because the high viscosity of silica-rich melt results in large viscous forces, relative to capillary forces (Klug & Cashman, 1996; Nguyen et al., 2013; Proussevitch et al., 1993). The emergent network of interconnected bubbles renders the magma permeable, with relatively small increases in porosity strongly enhancing bubble connectivity and leading to large increases in permeability. It is thought that shear deformation of the ascending magma, presumably most pronounced near conduit walls (e.g., Gonnermann & Manga, 2007; Mastin, 2005), will deform bubbles and thereby enhance bubble coalescence (Namiki, 2012; Okumura et al., 2009). For explosively erupted magmas there is a complete lack of low-porosity samples and all samples analyzed to date have been permeable; however, a porosity threshold is consistent with experimentally vesiculated samples (e.g., Burgisser & Gardner, 2005; Burgisser et al., 2017; Lindoo et al., 2016; Takeuchi et al., 2009). To complicate matters further, it has been suggested that permeability is hysteretic (Michaut et al., 2009; Rust & Cashman, 2004). This means that permeability depends on the history of magma vesiculation and for a given porosity permeability will have different values, depending on the direction of change in porosity.

The main objective of this paper is to test the hypothesis of permeability hysteresis. Instead of porosity-permeability relations obtained from samples across a variety of different eruptions, we focus on a single eruption, the 1060 Common Era (CE) Glass Mountain (GM) eruption of Medicine Lake Volcano, California, which encompasses both explosive and effusive phases. We first establish porosity-permeability relations for a suite of pyroclastic pumice from the Plinian phase of the eruption, which are of high porosity (on average between 0.7 and 0.8). We subsequently examine experimentally how porosity and permeability of these samples change during compaction and compare our results to data from other explosive and effusive eruptions, as well as other laboratory experiments. Unless magma is pervasively fractured, pore-scale flow is expected to be rate limiting during outgassing (Castro, Cordonnier, et al., 2012; Castro et al., 2014). We therefore focus on the development of permeability in the absence of magma fracturing, which may occur during shear deformation of the erupting magma (Castro, Cordonnier, et al., 2012; Castro et al., 2014; Gonnermann & Manga, 2003; Kushnir et al., 2017; Schipper et al., 2013; Tuffen et al., 2003, 2008) and also during compaction of dome lavas (Ashwell et al., 2015; Gonnermann & Manga, 2005; Tuffen et al., 2008). We thus develop a functional relation for the change in permeability with respect to porosity that is suited for numerical modeling of open-system magma degassing.

2. Geological Context

The Glass Mountain eruption was the last event of the postglacial eruptive activity of Medicine Lake Volcano, California (Anderson, 1933; Donnelly-Nolan et al., 2007, 2008; Heiken, 1978). The eruption consisted of a Plinian phase, during which crystal-free rhyolitic pumice erupted, followed by the emplacement of produced a lava flow, with a total erupted volume of approximately 1 km^3. The Plinian phase produced a fallout deposit of 0.27 km^3 dry rock equivalent, consisting of poorly sorted rhyolitic lapilli with no evidence for deposition by pyroclastic flows (Heiken, 1978). All pumices are essentially phenocryst-free (<5%, Heiken, 1978), with a microlite content of approximately 3 vol% (Stevenson et al., 1996), and texturally homogeneous.

The chemical composition of the tephra is similar to that of the Glass Mountain flow and has a SiO_2 content of approximately 72–75 wt% (Anderson, 1933; Heiken, 1978; Grove & Donnelly-Nolan, 1986; Grove et al., 1997). Magmatic inclusions and experimental petrologic studies indicate that the Glass Mountain magma formed under near H_2O-saturated conditions at pressures of 100–200 MPa (Grove et al., 1997), equivalent to depths of 3–6 km and initial magmatic water content of about 4–6 wt% (Liu et al., 2005). In agreement
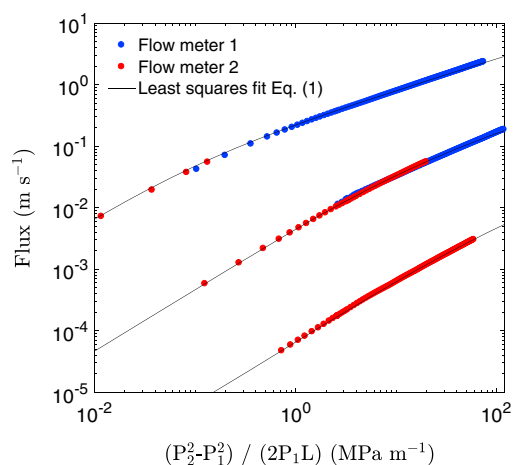
Figure 1. Examples of permeability measurements. Air flux as a function of pressure gradient for samples BGM-P-A2A-4 ($\log_{10} k = -14.91$, with k in units of m²), BGM20-3 ($\log_{10} k = -13.19$), and BGM20-4 ($\log_{10} k = -10.89$), together with least squares fits to estimate permeability coefficients k, k^*, and α in equation (1).

with these petrological and geochemical studies, seismic tomography has identified a silicic magma body of up to few tens of cubic kilometers volume at 3–7 km below the eastern part of Medicine Lake caldera (Chiarabba et al., 2012; Donnelly-Nolan et al., 2008; Evans & Zucca, 2012).

3. Analysis of Plinian Fall

3.1. Vesicularity Measurement

Twenty-four representative pumice clasts from the Plinian phase of the Glass Mountain eruption were collected across a wide stratigraphic range of the fallout deposit, located near the northern margin of the Glass Mountain flow. Clasts vary in size and reach up to 0.30 m in diameter. They are phenocryst free and isotropic, showing no obvious vesicle orientation or gradients in porosity or vesicle size. Depending on clast size, one or several cores, 0.02 m in diameter, were drilled from each clast and then cut to produce samples of 0.01–0.02 m length, resulting in a total of 76 samples with approximate aspect ratio of 1:1 for porosity and permeability analysis. The envelope volume of each sample, V_t, was estimated using the average of 10 measurements of the length and diameter of the cylinder obtained with a digital caliper. The sample was then weighed to determine its mass, M_t. The skeletal volume, V_s, that is solid matrix plus isolated vesicles not accessible by gas was obtained using a He-pycnometer (AccuPyc II 1340, Micromeritics Instrument Corporation). Together with the envelope volume, V_t, that is solid matrix plus all vesicles, V_s was used to calculate the connected, helium-accessible volume, $V_t - V_s = V_c$. From the ratio of V_c and V_t we calculated the connected vesicularity, ϕ_c, for each sample. Part of the sample not used for permeability analysis was finely crushed, the powder was weighed, and the powder volume was determined using the helium pycnometer. From these we calculated an average matrix density of $\rho_m = 2,430$ kg m^{-3}. For each sample we calculated the matrix volume $V_m = M_t/\rho_m$ and the total vesicularity, $\phi_t = (V_t - V_m)/V_t$, of the sample.

3.2. Permeability Measurement

The cylindrical samples produced during the vesicularity analysis were mounted on plexiglas and sealed with high-viscosity epoxy along the radial perimeter, so that air flow during permeability measurements was in the axial direction. Because of the high viscosity of the epoxy and its short curing time, we see no evidence for significant imbibition of epoxy in microtomographic images of select samples. The volumetric flow rate of laboratory air through the sample was measured at different inlet pressures using a capillary flow porometer (Model CFP-1100AXL-AC, Porous Media, Inc.). The maximum applied pressure difference for any sample was 0.5 MPa resulting in volumetric flow rates over a range of approximately 1 to 2 orders of magnitude, measured using several flow meters, each accurate over a different range of flow rates, and ranging from the minimum detection limit of 3×10^{-8} m³ s^{-1} to less than 3×10^{-3} m³ s^{-1} (Figure 1). For a cylindrical sample of 0.02 m in length and 0.01 m in radius, which is the average size of our samples, the minimum measurable Darcian permeability was approximately 10^{-17} m². Given the nonlinear relation between pressure difference and flow rate of these samples, the maximum measurable permeability exceeds any values reported herein.

Inertial effects can be significant when measuring the permeability of volcanic rocks at high flow rates (Degruyter et al., 2012; Rust & Cashman, 2004; Takeuchi et al., 2008), requiring what is known as Forchheimer's correction to Darcy's law (Forchheimer, 1901; Lasseux & Valdés-Parada, 2017, and references therein). Furthermore, for compressible gases the gas permeability may differ from the liquid permeability of the same material, requiring what is known as the Klinkenberg slip correction (Klinkenberg, 1941; Lasseux & Valdés-Parada, 2017, and references therein). For each sample we assessed the requirement for each correction by estimating values of k, the Darcian permeability, k^* the Forchheimer coefficient (non-Darcian permeability), and α, the Klinkenberg slip factor, using

$$\frac{P_2^2 - P_1^2}{2P_1 L} = \frac{\eta_g}{k\left(1 + \alpha/P_{avg}\right)}q + \frac{\rho_g}{k^*}q^2, \tag{1}$$
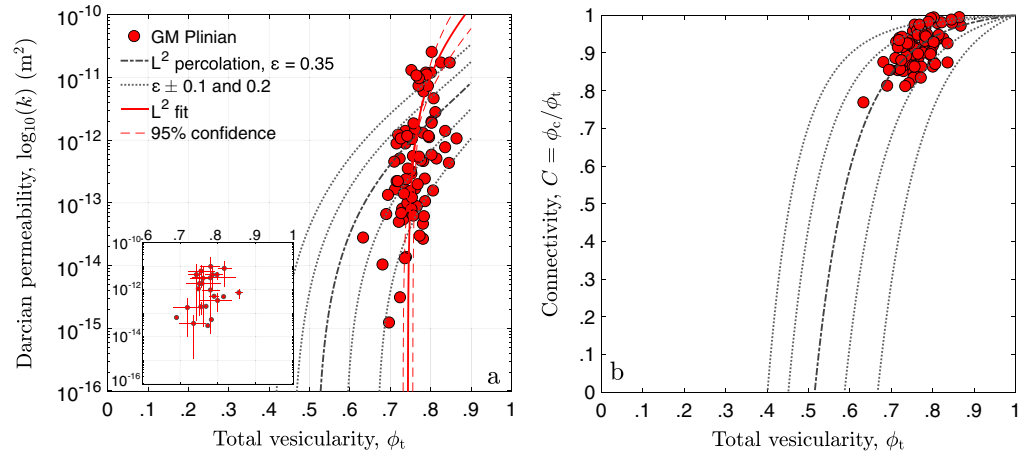
Figure 2. (a) Darcian permeability, k, vs. total porosity, ϕ_t, for individual cores taken from the Glass Mountain pumice clasts (Plinian fall). Measurement limit on k is approximately 10^{-17} m^2. The red curve represents the least squares fit to the measured values of ϕ_t as a function of k, based on equation (2), with dashed red curves showing the 95% confidence interval. Inset shows the range in values obtained from multiple cores of the same clast with the mean value of $\log_{10}(k)$ and ϕ_t shown as filled circles and the vertical and horizontal bars indicating the range in values for the given clast. (b) Corresponding connectivity, C, versus total porosity, ϕ_t. The solid gray curve is the least squares fit to ϕ_c as a function of ϕ_t obtained from percolation modeling with $\varepsilon = 0.35$, corresponding to estimated values of $\phi_{cr} = 0.52$, $b = 0.42$, and $n = 2.87$. Also shown as gray dashed curves are results from percolation modeling for $\varepsilon = 0.15, 0.25, 0.45$, 0.55, corresponding respectively to $\phi_{cr} = 0.40, 0.45, 0.59$, and 0.66, as well as $b = 1.04, 0.69, 0.22, 0.13$, and $n = 3.21, 3.07$, $2.66, 2.49$.

where P_2 and P_1 are the inlet and outlet pressures, respectively, and $P_{avg} = (P_2 + P_1)/2$. Furthermore, q is the volumetric flow of air per sample cross-sectional area (i.e., the volume flux of air), L is the length of the sample, $\eta_g = 1.86 \times 10^{-5}$ Pa s, and ρ_g are respectively the viscosity and density of the air, with the latter approximated as an ideal gas with $\rho_g = 1.18$ kg m^{-3} at $P = 1$ atm. We find that all samples require a Forchheimer correction, whereas a Klinkenberg slip correction does not improve the fit and the estimated value for α is ≪1 Pa. Figure 1 provides an illustrative example of flow rate data and best fits using equation (1).

3.3. Porosity and Permeability Values (Plinian)

Results of the porosity and permeability analyses of the Glass Mountain pumices are provided in Figure 2 and Table A1. All estimated permeabilities are at least 2 orders of magnitude larger than the detection limit of 10^{-17} m^2. Furthermore, all samples show a high ratio of connected to total porosity, defined as connectivity, $C = \phi_c/\phi_t$.

Each data point shown in Figure 2 corresponds to an individual core taken from a set of clasts, whereas the inset to Figure 2a shows the mean and the range in values for all cores from a given clast. It indicates a large degree of heterogeneity in permeability at the centimeter scale.

Similar to other porous materials, the permeability of vesicular volcanic rocks can be assessed within the framework of percolation theory (e.g., Blower, 2001a, 2001b), yielding a power law to describe the relationship between k and ϕ_t

$$k = a\, r^2 \left(\phi_t - \phi_{cr}\right)^n = b \left(\frac{\phi_t}{(1-\phi_t)}\right)^{2/3} \left(\phi_t - \phi_{cr}\right)^n. \tag{2}$$

Here b, n, and ϕ_{cr} are fitting parameters. r is the average vesicle radius, which for a given bubble number density, N, is dependent on porosity as

$$r^3 = \frac{3}{4\pi N} \frac{\phi_t}{1 - \phi_t}. \tag{3}$$

ϕ_{cr} is called the percolation threshold, which is defined as the porosity below which permeable flow is not possible, because no interconnected pore space spans the entire sample. These parameters can be estimated by fitting a function $\phi_t = f(k)$. This is the solid red curve in Figure 2 obtained from a least squares fit to equation (2) with an assumed value of $n = 2$, resulting in $\log_{10}(b) = -8.892\,(\pm 0.837)$, $\phi_{cr} = 0.7436\,(\pm 0.0243)$ and a root-mean-square error in ϕ_t of 0.037. It should be noted that a wide range of values $n \geq 1$ will
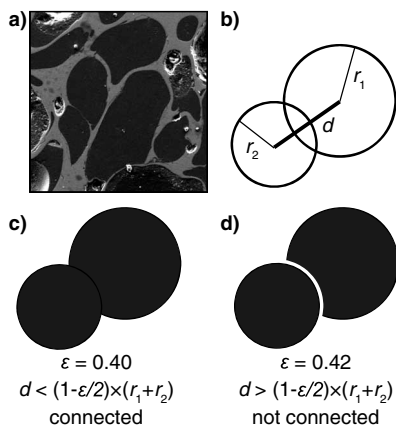
Figure 3. Illustration of the geometrical parameter ε used in the percolation model (Blower, 2001a, 2001b). (a) SEM image of a Glass Mountain pumice showing that vesicles can be nonspherical, representing deformed bubbles that were separated by thin films of melt. (b) Two overlapping spheres of radii r_1 and r_2. (c) At a value of $\varepsilon = 0.40$, corresponding to $d < (1 - \varepsilon/2) \times (r_1 + r_2)$, the two spheres are considered connected (coalesced) and gas can flow between them. (d) At a value of $\varepsilon = 0.42$, corresponding to $d > (1 - \varepsilon/2) \times (r_1 + r_2)$, the two overlapping spheres are considered isolated and gas cannot flow between them.

Figure 4. (a) Backscattered scanning electron microscope image of a typical fallout Plinian pumice from the Glass Mountain eruption. Vesicles appear in dark gray and the glass in light gray. (b) Vesicle number (black) and volume (red) fractions obtained by image analysis. Number density is dominated by vesicles with a radius <5 μm, while volume is dominated by vesicles 20–50 μm. The average vesicle radius is 12.1 μm.
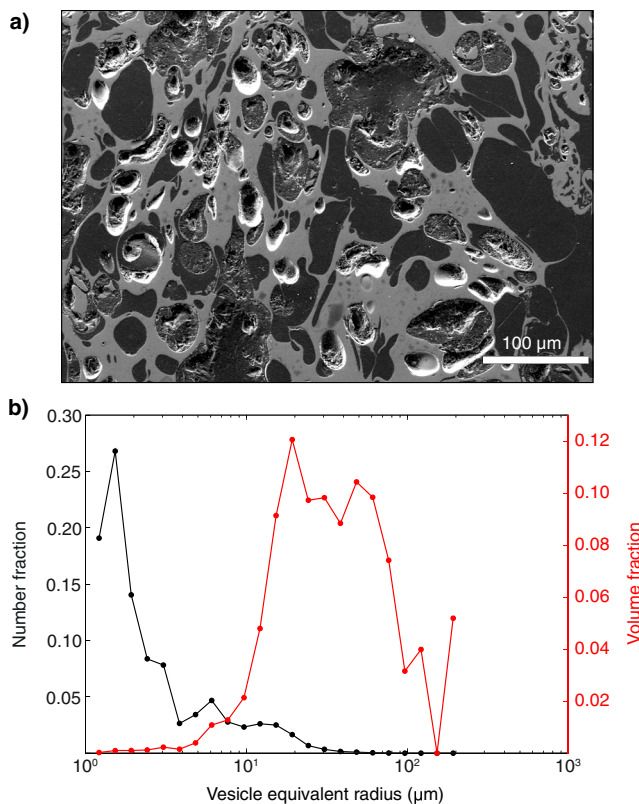
give similar fits to the data with little variability in root-mean-square error and variations in ϕ_{cr} of approximately ± 0.01, but significantly different values of b.
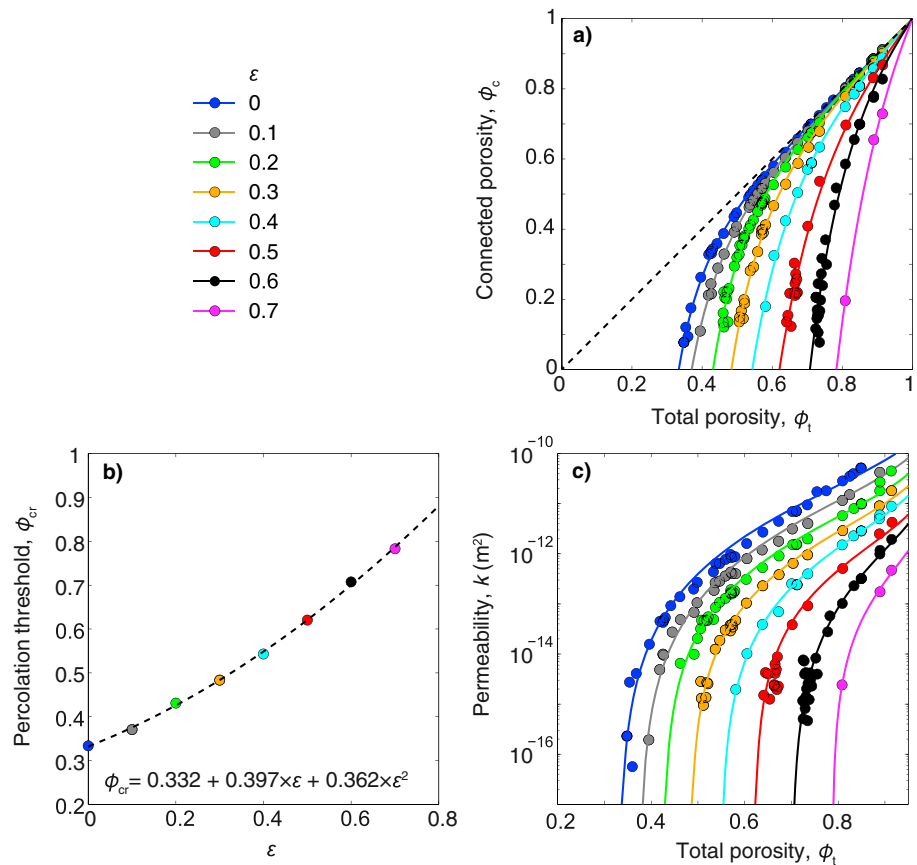
3.4. Percolation Modeling (Plinian)

An alternative to fitting the data with a power law is fitting the measured values of ϕ_t and ϕ_c, using a percolation model. In this manner one can also obtain a functional relation between k and ϕ_t, shown as the solid gray curve in Figure 2. The percolation model is based on the assumption that the complex network of vesicles within a pumice can be reproduced by spheres that are randomly distributed in a volume. Any two spheres that overlap are assumed to be interconnected (Blower, 2001a, 2001b). At some threshold volume fraction, ϕ_{cr}, enough spheres will be interconnected to create a percolating cluster, defined as network of interconnected spheres that spans the entire length of the sample, in principle allowing fluid flow through the sample from one end to the other.

The percolation model used spheres drawn at random from a size distribution equal to the vesicle size distribution of a representative Glass Mountain sample, in order to account for the effect of polydispersivity on ϕ_{cr} (Blower, 2001b; Mecke & Seyfried, 2002). Each sphere was randomly placed in a cubic volume of 10^{-8} m^3 until a total porosity of the modeled volume, ϕ_t, was reached. If the centers of two spheres of radii r_1 and r_2 are separated by a distance less than $(1 - \varepsilon/2) \times (r_1 + r_2)$, where $0 \leq \varepsilon \leq 1$, the two spheres are considered connected (Blower, 2001a, 2001b). The parameter ε can be chosen arbitrarily. It determines the extent to which two adjacent spheres must overlap before they are considered to be connected through coalescence (Figure 3). The use of ε is based on the observation that growing bubbles may impinge upon one another and deform, but remain separated by a thin film of melt (Figure 3a). ε thus accounts for the fact that spheres in the percolation model cannot deform, allowing them to be modeled as unconnected (Figures 3b–3d), in analogy to deformed but noncoalesced bubbles that would overlap if they were spherical. Everything else being equal, a higher value of ε leads to less connected spheres, a higher percolation threshold, and a lower permeability. Overlapping spheres thus create clusters from which the connected porosity, ϕ_c, was calculated. For each cluster that spanned from one end of the sample to the other, defined as a "percolating cluster," permeability was calculated by assuming that flow resistance across the cluster depends on the size and number of apertures between individual bubbles, equivalent to a network of resistors (Blower, 2001a, 2001b).

The vesicle size distribution from which spheres were drawn was obtained by image analysis from a representative Glass Mountain pyroclast with $\phi_t = 0.75$ and $\phi_c = 0.66$ (BGM20, Table A1). The sample was thin sectioned and scanning electron microscope (SEM) images of this section were taken at magnifications of 80X (one image) and 300X (three images). These grayscale images (Figure 4a) were manually transformed into binary images and vesicle walls were reconstructed if two adjacent vesicles are interpreted to represent coalesced bubbles (e.g., Giachetti et al., 2010; Toramaru, 1990). The images were then analyzed using the program FOAMS (Shea et al., 2010). We used a minimum resolvable diameter of 5 pixels, which corresponds to a vesicle of approximately 2.4 μm on the 300X images. A minimum resolvable diameter of 5 pixels for this type of highly porous pyroclast allows to discard noise in the data while maintaining an uncertainty on the vesicle number density of about 5% (Shea et al., 2010). The analysis of 2,250 vesicles on SEM images gave a vesicle number

Figure 5. Results from the percolation model (circles) for $0 \le \varepsilon \le 0.7$. (a) Connected porosity, ϕ_c, as a function of total porosity, ϕ_t, and least squares fit using equation (4), with $1.5 \times 10^{-3} \le \beta \le 257 \times 10^{-3}$ and $4.45 \le \gamma \le 6.89$, both depending on the value of ε. (b) ϕ_{cr} as a function of ϕ_t and least squares fit using equation (5). (c) Permeability, k, as a function of ϕ_t and least squares fit using equation (2).

density of 4×10^{14} m^{-3} per volume melt and an average vesicle radius of 12.1 μm, similar to Plinian pumices from other eruptions (Figure 4b) (Adams, Houghton, & Hildreth, 2006; Klug et al., 2002; Rust & Cashman, 2011; Shea et al., 2012, 2014). The maximum vesicle radius is about 200 μm and vesicles within 20–50 μm constitute the majority of the porosity.

Because the calculation time for the percolation modeling increases exponentially with the number of spheres, only spheres of size ≥ 10 μm were modeled. This choice is justified by the fact that vesicles with a radius <10 μm represent a porosity of approximately 0.06, but account for about 90% of the vesicle number density. Moreover, most of the smallest vesicles are likely isolated (e.g., Giachetti et al., 2010; Klug et al., 2002). If connected, their contribution to sample permeability is expected to be small because permeability scales with the square of vesicle radius (e.g., Saar & Manga, 1999; Blower, 2001a, 2001b).

In the percolation model the value of ϕ_t may be varied by changing the number of bubbles or their radius (Blower, 2001a). We find that both approaches yield similar results, provided that the domain size is greater than 10 times the largest bubble radius (Blower, 2001a), and we varied ϕ_t by changing the average bubble radius. For a given value of ε we generated repeated realizations of the percolation model with different ϕ_t and corresponding values of ϕ_c and k. For each value of ε, we then estimated ϕ_{cr} by finding the best fit of ϕ_c as a function of ϕ_t, using the functional relation

$$\phi_c = \phi_t + \beta \left(1 - \frac{1}{\phi_t^\lambda} \right), \tag{4}$$
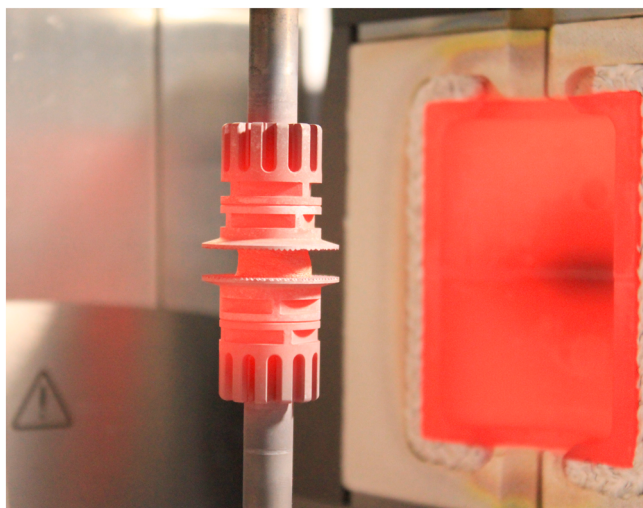
Figure 6. Sample during deformation photographed after opening oven at a temperature of 975°. During the deformation experiment the oven is closed. A stable and uniform sample temperature is achieved through a thermal control system. Shown are rotating upper shaft and stationary lower shaft, both with serrated plates attached, and the deforming sample in between. The lower shaft includes an internal thermocouple. To the right of the sample is one half of the glowing opened oven.

where β and λ are fitting parameters. The results are shown in Figures 5a and 5b, where the functional relation between ϕ_{cr} and ε can be approximated by

$$\phi_{cr} = 0.332 + 0.397\varepsilon + 0.362\varepsilon^2. \tag{5}$$

Using the value of ϕ_{cr} obtained from fitting of ϕ_c, we then find the best fit of k as a function of ϕ_t, assuming that equation (2) applies. As shown in Figure 5c, the results for each value of ε correspond to unique values of ϕ_{cr}, b, and n in equation (2) from which we obtain functional relations for b and n with respect to ε.

A comparison of the predicted relationships of ϕ_c versus ϕ_t and k versus ϕ_t with the measured values for the Glass Mountain samples is shown in Figure 2. The fits that can be obtained from percolation modeling tend to be biased toward lower values of the parameters b and n in equation (2), compared to those obtained by direct fitting of k and ϕ_t. The narrow range in ϕ_t over which all samples are permeable makes it difficult to constrain ϕ_{cr} (Figure 2a). This is also reflected in the clustering of ϕ_c versus ϕ_t data (Figure 2b). Although a value of ϕ_{cr} as low as 0.4, or perhaps even less, is required to match samples with high connectivity, other samples require considerably higher values of ϕ_{cr}. The remarkably narrow range in ϕ_t can perhaps be explained best as a reflection of the conditions at which the magma fragmented. The simplest explanation for the correspondingly wide range in k would be inherent heterogeneity in connectivity and permeability, at least at the scale of individual pyroclasts (Figure 2a). Alternatively, it is simply a matter of preservation, with impermeable parts of the magma fragmenting to ash size (Rust & Cashman, 2011).
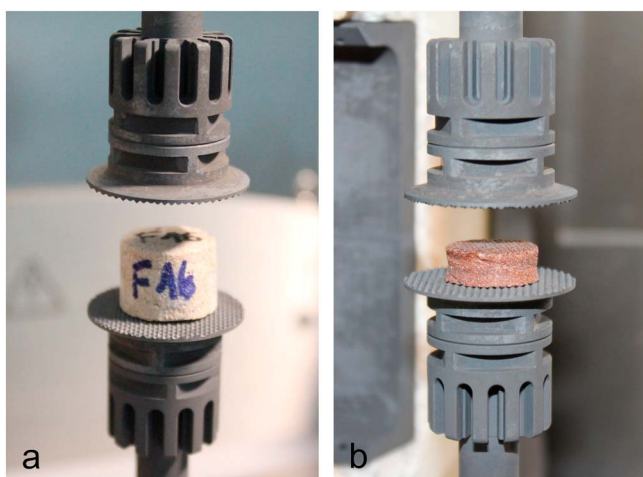
4. Outgassing Experiments

4.1. Objective and Methodology

To better understand how permeability changes if the magma undergoes compaction and shear deformation, as it presumably does during effusive eruptions, we took a subset of the Plinian Glass Mountain clasts and deformed them under combined compression and shear. Individual samples were mounted between two serrated parallel plates attached to an Anton Paar MCR301 rheometer and placed inside a temperature-controlled oven preheated to 975° (Figures 6 and 7). Before deformation samples were held for longer than the characteristic thermal diffusion time ($\sim$100 s) to assure thermal equilibration (Bagdassarov & Dingwell, 1994). Throughout the experiments temperature was held constant and measured by a thermocouple installed within the lower plate. Based on design specifications, thermal gradients across the sample were negligible and measured temperatures varied by less than 1° throughout the deformation experiments.

A normal force of $\sigma = 2$ N and a torque of $\Gamma = 1.07 \times 10^{-2}$ N m^{-1} were applied for a specified time between approximately 10 and 300 min. This resulted in a range of total shear strain, γ, and axial strain, ε, as shown in Table A2, as well as maximum shear rates of 9×10^{-3} s$^{-1} < \dot{\gamma} < 8 \times 10^{-6}$ s^{-1}, depending on sample diameter, and calculated as

$$\dot{\gamma}(r=R) = \frac{R\Omega}{L}, \tag{6}$$

Figure 7. Illustrative example of sample before and after deformation: (a) BGM-20-2 before deformation and (b) after deformation of approximately 313% shear strain and 59% axial strain. The sample is typical of all samples. The change in color is due to sample oxidation. No barreling was observed. Axial ends that were in contact with the serrated plates were carefully sanded to assure that porosity and permeability measurements were not affected by deformation of the sample surface due to the serrated plates.

where $\dot{\gamma}(r)$ is the shear rate at radius $0 \leq r \leq R$. Furthermore, R is the sample radius, Ω is the rotation rate, and L is the axial length of the sample. The resultant range in apparent viscosities was approximately 10^{10} Pa s to 10^{12} Pa s. At all times shear rates were below the onset of non-Newtonian behavior, as defined by Webb and Dingwell (1990) for rhyolite from Medicine Lake Volcano. Simultaneously to shear deformation,

Figure 8. Combined data from Plinian samples and deformation experiments. (a) Darcian permeability, k, versus total porosity, ϕ_t, for Glass Mountain Plinian fall (red filled circles), which is the same as shown in Figure 2, together with a subgroup of the same samples after compaction and shear deformation (blue filled circles). Lines connect each pair of undeformed-deformed samples. Measurement limit on k is approximately 10^{-17} m². (b) Corresponding connectivity, ϕ_c/ϕ_t, versus total porosity, ϕ_t.

an axial force of $\sigma = 2$ N was applied to each sample. This corresponds to stresses of approximately 1×10^4 Pa to 2×10^4 Pa and resulted in average axial shortening rates of $\dot{\epsilon} \sim 10^{-4}$ s^{-1}, which is at the lower end of experimental conditions of, for example, Bagdassarov and Dingwell (1992). At the end of the experiment the sample was cooled at a rate of approximately $0.5° $ s^{-1}. To assure that samples did not fracture during deformation or cooling, we inspected a subset of samples using computed microtomography (section 4.3).

The shear strain γ can be calculated from the sample radius, length, and the cumulative deflection angle, θ, recorded by the rheometer, as

$$\gamma = R\frac{\theta}{L}. \tag{7}$$

The shear stress, τ, was calculated as

$$\tau = \frac{\Gamma}{\pi R^3} \tag{8}$$

and the shear rate, $\dot{\gamma}$, as

$$\dot{\gamma} = \frac{\Omega R}{L}. \tag{9}$$

The axial strain, ϵ, is the Cauchy or engineering strain, calculated from the initial sample length, L_i, and the final length, L_f, as

$$\epsilon = \frac{L_f - L_i}{L_i}. \tag{10}$$

Both L and R changed during the experiment. Whereas L is measured by the rheometer, the value of R as a function of time was estimated assuming a constant rate of change between initial and final value, which is reasonable because overall the sample radii changed only by small amounts (Table A2).

4.2. Porosity and Permeability After Deformation
We followed the procedure outlined in section 3 to measure porosity and permeability after sample deformation, with the flow directed along the axis of the cylindrical core. The results are shown in Figures 8 and 9, as well as tabulated in Table A3. Deformation decreased sample porosity between approximately 10% and 75%. Most deformed samples therefore have porosities that are lower than those observed in the undeformed Glass Mountain Plinian samples. The tie lines in Figure 8a connect undeformed samples (denoted by superscript [i] for "initial") and deformed samples (denoted by superscript [f] for "final"). If permeability development during expansion of the Plinian samples followed a trajectory with a high percolation threshold, as inferred by a power law relation between k and ϕ_t, then compaction of these samples was hysteretic with k at any given ϕ_t larger during compaction than during expansion, as first proposed by Rust and Cashman (2004).
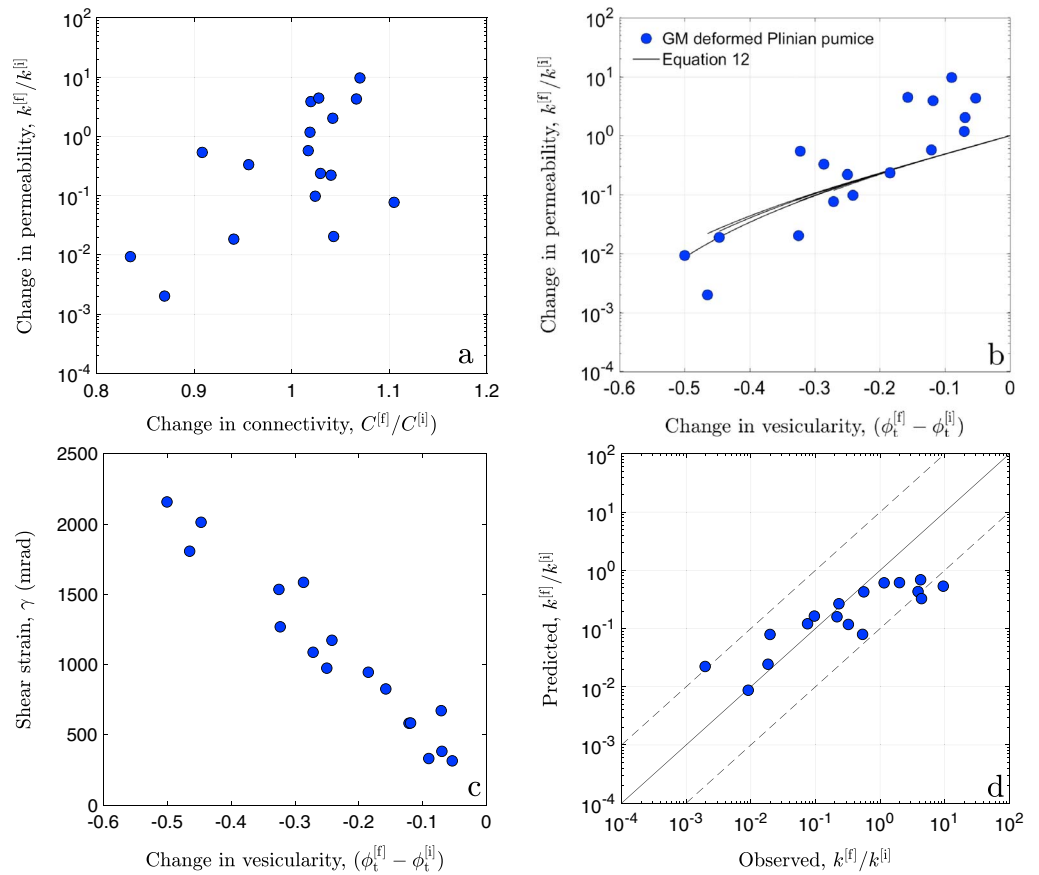
Figure 9. Data from deformation experiments. (a) Change in permeability, k, expressed as permeability ratio $k^{[f]}/k^{[i]}$, versus change in connectivity, C, expressed as connectivity ratio $C^{[f]}/C^{[i]}$. (b) Change in permeability versus change in vesicularity, $\Delta\phi_t = \phi_t^{[f]} - \phi_t^{[i]}$. Black curves are predictions from equation (11) with $n = 2.8$. (c) Shear strain, γ, versus change in vesicularity. (d) Predicted versus observed change in permeability based on equation (11), corresponding to the results shown in Figure 9b.

The change in permeability during compaction is likely due to two contributing factors: (i) decreasing vesicle size and (ii) change in connectivity. The required deformation of the melt can be due to applied , gravitational, and capillary stresses (Kennedy et al., 2016). The latter scale inversely with bubble radius (e.g., Castro, Burgisser, et al., 2012; Nguyen et al., 2013; Proussevitch et al., 1993; Toramaru, 1988). Because sample porosity is predominantly due to vesicles with a radius of about 10 μm to 100 μm (Figure 4), capillary stresses were predominantly in the range 10^3 Pa $\lesssim 0.1$ m N$^{-1}\times$ (vesicle radius)$^{-1} \lesssim 10^4$ Pa. Gravitational stresses were $\lesssim 10^3$ Pa, whereas the applied stresses were $\sim 10^4$ Pa. We conclude that the decrease in vesicle size and porosity were predominantly in response to the applied shear and axial stresses, albeit with a secondary contribution due to capillary stresses (Kennedy et al., 2016).

Our experiments indicate that after bubbles have become interconnected to form a permeable network, it may be difficult to significantly reduce connectivity during compaction (Figure 8b). Although the precise mechanism for this remains to be fully understood (e.g., Kennedy et al., 2016), during compaction samples appear to remain permeable to low porosities. Therefore, assuming $\phi_c = 0$ and no change in pore connectivity other than the decrease in vesicle size, the change in permeability can be obtain by differentiating equation (2), which gives

$$\frac{\mathrm{d}k}{\mathrm{d}\phi_t} = \left(n + \frac{2}{3}\right)\frac{k}{\phi_t} + \frac{2}{3}\frac{k}{(1 - \phi_t)}. \tag{11}$$

It should be noted that for $n = 1$, this is equivalent to assuming a Kozeny-Carman relation between permeability and porosity (e.g., Berryman & Blair, 1987; Klug et al., 2002).
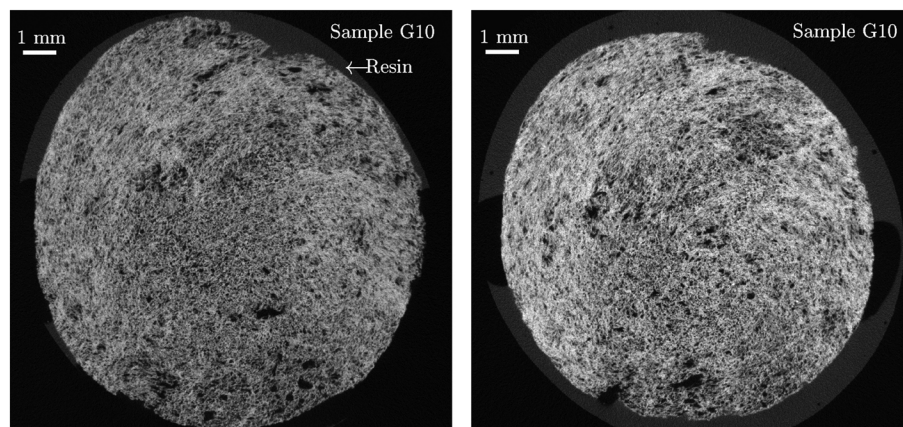
Figure 10. Illustrative examples of postdeformation microtomography images of sample BGM-P-A2m-3, taken at different axial positions and viewed perpendicular to the rotation axis. Note that there is no indication of fractures. Image resolution for left image is 8.7 μm per voxel and 1.95 μm per voxel for the right one. Darker colors are vesicles (pore space), whereas lighter colors are glass.

We have estimated parameter n in equation (11) by integrating this equation for each sample, from the initial (undeformed) value of porosity, $\phi_t^{[i]}$, and corresponding initial value $k^{[i]}$, to its final (deformed) value, $\phi_t^{[f]}$, while minimizing the root-mean-square error between the predicted and observed permeabilities of the deformed samples, $k^{[f]}$. The results are shown in Figure 9b and correspond to a value of $n = 2.8$. It is apparent that equation (11) is inadequate at fitting samples that have undergone only small degrees of compaction, some of which show an increase in permeability. It is in principle feasible to improve the fit by adding another term to equation (11) to account for increases in vesicle connectivity, for example, due to capillary forces (e.g., Kennedy et al., 2016), or due to bubble elongation, which has been shown to increase permeability and reduce the percolation threshold (e.g., Blower, 2001b; Garboczi et al., 1995; Xu et al., 2016; Yi & Sastry, 2004). At present we lack a sound theoretical foundation to derive such an additional term and we therefore refrain from speculating based on empirical considerations. Nevertheless, our results indicate that it may be difficult to substantially reduce connectivity through compaction. Moreover, in the early stages of deformation connectivity and permeability may even increase (Figures 8a and 8b).

4.3. Computed Microtomography

To ensure that measured permeabilities of the deformed samples are solely due to interconnected vesicles, as opposed to fractures (e.g., Ashwell et al., 2015; Heap & Kennedy, 2016; Kushnir et al., 2017), we imaged several samples using X-ray computed microtomography. The imaged samples, BGM-P-1B-1, BGM6-8, and BGM-P-A2m-3 (Figure 10a), cover a wide range of shear strain (Table A2) and were analyzed at the High-Resolution X-ray Computed Tomography Facility, University of Texas, Austin. The resolution used was 8.7 μm per voxel, obtained at 100 kV, 10 W, and with a 4 s acquisition time, producing a stack of 440–550 regularly spaced images per sample. Additionally, a scan of the center of sample BGM-P-A2m-3, which experienced the largest deformation, was also made at a resolution of 1.95 μm per voxel using 110 kV, 10 W, and 5 s acquisition time (Figure 10b).

The stack of low-resolution images was analyzed using the 3-D analysis plug-in of the Fiji image analysis software (Ollion et al., 2013; Schindelin et al., 2012) with a cut-off in vesicle size of >50 voxels (Giachetti et al., 2011), corresponding to a minimum equivalent sphere diameter of approximately 40 μm. The 23,768 vesicles thus analyzed represent a porosity of 2.4%, accounting for about 7.4% of the 33.0% final porosity of the sample. They have an average aspect ratio of approximately 3.2 ± 0.4, are on average preferentially oriented at an angle of $65 \pm 8°$ from the deformational axis of rotation, and show increasing elongation and alignment with distance from the rotation axis. Any fracture at least 2-voxel wide (i.e., about 20 μm on the low-resolution images and 4 μm on the high-resolution ones) should be visible in the scans; however, none were detected. We therefore believe that the permeability of our samples is due to interconnected vesicles.

5. Comparison to Other Data

To provide broader context, we compare the Glass Mountain data to porosity and permeability data from (1) fall deposits of other high-silica Plinian eruptions; (2) high-silica dome and flow samples; (3) vesiculation experiments; and (4) other shear deformation experiments. These data are summarized in Figures 11 and B1. One objective of the data comparison was to assess the variability among rhyolitic Plinian pyroclasts across a range of eruption intensities, with the Glass Mountain samples representing the lowest intensity. A second objective was comparing our compacted samples to natural rhyolitic samples that are thought to have undergone compaction and shear deformation. Lastly, we hope to provide the reader with additional information related to the existence of a percolation threshold. Given these objectives, we refrain from attempting a comprehensive compilation of published porosity-permeability data.

5.1. Natural Samples

The following "natural" high-silica samples were included for comparison to the Glass Mountain samples:

1. Plinian fall from Little Glass Mountain represents an explosive phase similar age and close proximity to the Glass Mountain samples (Rust & Cashman, 2004).
2. Plinian fall from the 7.7 ka climactic eruption of Mount Mazama formed Crater Lake caldera, Oregon (CLCP samples of Klug & Cashman, 1996) and (Klug & Cashman, 1996, excluding the Welded Tuff samples).
3. Plinian fall from Episodes I–III of the 1912 eruption of Novarupta, Alaska (Adams, Houghton, Fagents, & Hildreth, 2006; Adams, Houghton, Hildreth, 2006; Fierstein & Hildreth, 1992; Hildreth & Fierstein, 2000, 2012), where mass eruption rates of approximately 5, 1.6, and 1.1×10^8 kg s^{-1}, respectively, provide a powerful Plinian reference (Nguyen et al., 2014).
4. "White microvesicular," crystal-poor, rhyolitic Plinian fall from the "Taupo Plinian" (Table A4), which is Unit 5 of the 181 CE Taupo eruption, New Zealand (Houghton et al., 2010, 2014), and provides another high-intensity Plinian reference with discharge rates of about 10^8 kg s^{-1} and plume heights between 25 and 37 km.
5. Fall from the bottom part of Unit I of the Upper El Cajete member of Valles Caldera, New Mexico (e.g., Wolff et al., 2011; Self et al., 1988) represents an eruption column that may have been in a transitional regime between fall- and flow-producing conditions (Wolff et al., 2011) and therefore constitutes a distinct end-member regime of activity within the suite of Plinian samples (Table A5).
6. Pumices from the 0.76 Ma Bishop Tuff ignimbrite, Long Valley Caldera, California, were collected in the unconsolidated, extremely poorly sorted, whitish pumice-rich Sherwin subunit of Ig1Eb (Hildreth & Wilson, 2007; Wilson & Hildreth, 1997). Although no estimate of mass discharge rate exists for the caldera-forming phase of the eruption itself, the mass discharge rate of the precaldera Plinian phase peaked at about 7.5×10^8 kg s^{-1} (Gardner et al., 1991). These samples were deposited from pyroclastic density currents and therefore provide a caldera-forming, high-intensity reference (Table A6).
7. Rhyolitic (Swanson et al., 1989) dome samples from the 600 year old Obsidian Dome, California, were the basis for the original outgassing hypothesis by Eichelberger et al. (1986).
8. Samples from Little Glass Mountain and Glass Mountain lava flows represent a later phase of the same eruptions that produced the Glass Mountain Plinian samples (Donnelly-Nolan et al., 1990). Some of the samples were analyzed by Rust and Cashman (2004) and additional samples were analyzed by us (Table A7).
9. The 1912 Novarupta, Alaska, Episode V formed a lava dome and provides another effusive reference (Nguyen et al., 2014).

5.2. Experimental Samples

We include two sets of experimentally vesiculated, crystal-free, rhyolitic samples for which porosities and permeabilities have been measured. They include rhyolitic melts experimentally vesiculated by decompression from 180 MPa (approximately 4.7 wt% dissolved H_2O) to 5–30 MPa at rates of 0.002–0.05 MPa s^{-1} (Takeuchi et al., 2009), as well as data from Lindoo et al. (2016) who performed decompression experiments with rhyolitic melts (76.32% SiO_2) that were hydrated at 150 MPa and decompressed at 0.25 MPa s^{-1} to pressures between 15 and 125 MPa. We also include samples from Okumura et al. (2009) who measured permeability and porosity of samples obtained from torsional deformation experiments of vesiculated rhyolitic melts at shear rates of <0.029 s^{-1} up to a total strain of 34.6. The samples were natural obsidian from Wadatouge, Japan, with 0.77 wt% SiO_2 and 0.5 wt% dissolved H_2O. Prior to deformation, samples were vesiculated by holding them at 975° for 5–15 min. Permeabilities were measured parallel and perpendicular to the shear direction.
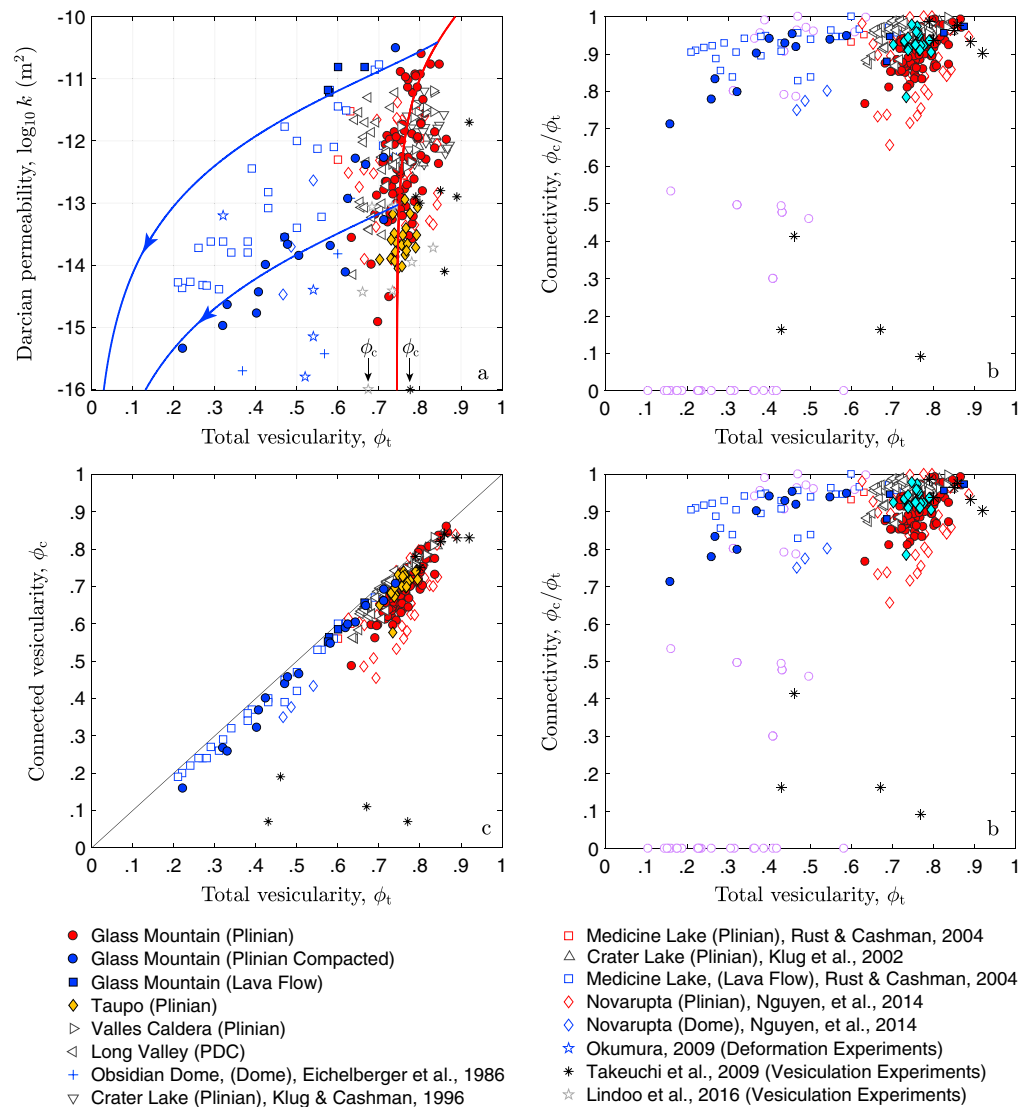
Figure 11. Data from Glass Mountain samples, other explosive and effusive eruptions, and experiments. (a) Log of Darcian permeability, k, as a function of total vesicularity, ϕ_t. The red curve represents the fit to Glass Mountain Plinian data (equation (2)) and the blue curves are based on equation (11). The arrows labeled ϕ_{cr} indicate the maximum value of ϕ_t for which permeabilities were below the detection limit ($\sim 10^{-17}$ m^2 for Takeuchi et al., 2009 and $< 10^{-15}$ m^2 for Lindoo, 2016). (b) Connectivity, ϕ_c/ϕ_t, as a function of total porosity. (c) Connected volume fraction of vesicles, ϕ_c, versus total porosity. (d) Log of Darcian permeability as a function of connectivity. Note the outliers in Figures 11b and 11c are for experiments with undetectable permeabilities.

The permeability detection limit for these experiments was at about 10^{-16} m^2, and only values for samples with permeabilities above the detection limit are shown. These data provide a useful comparison to the deformed Glass Mountain samples because they used crystal-free rhyolitic obsidian as the starting material.

6. Discussion

6.1. Permeability During Expansion

The Glass Mountain Plinian samples overlap extensively with Plinian fall from other silicic eruptions (Figure 11). All samples are permeable and span a narrow range in porosity, but with a wide range in permeability. Although samples from other eruptions also span a wide range in permeability, the Taupo samples occupy a comparatively narrow range. Systematic large-scale spatial variations within the conduit, or variations in eruption dynamics over time, are thought produce variability in properties of the erupted magma

(e.g., Adams, Houghton, Fagents, & Hildreth, 2006; Adams, Houghton, Hildreth, 2006), for example, in porosity, vesicle texture and presumably also in permeability. We find that permeability of individual Glass Mountain pyroclasts can be variable at the centimeter scale (Figure 2a). We therefore surmise that much of the overall variability in permeability may be attributable to centimeter-scale heterogeneity within the magma.

We have seen no evidence for pervasive breaking of bubble walls during sample preparation or analysis, and it has been suggested that the complete lack of impermeable, or for that matter low porosity, Plinian samples is a consequence of impermeable magma fragmenting into ash-size particles, because excess gas pressure cannot be dissipated by permeable flow (Rust & Cashman, 2011). An alternative possibility, which we favor, is that the narrow range in porosity of the explosive samples shown in Figure 11 simply indicates the porosity at which fragmentation conditions were reached (Gonnermann, 2015; Papale, 1999; Sparks, 1978) and that the lack of impermeable samples indicates that the magma had become pervasively permeable. Lastly, the decompression experiments shown in Figure 11 complement the natural samples with low-porosity data. They support the prediction that vesiculating magma can remain impermeable up to a threshold in porosity, likely the consequence of limited time for bubble coalescence during magma ascent (Martel & Iacono-Marziano, 2015).

6.2. Permeability During Compaction

The relationship between permeability and porosity for crystal-free, effusive silicic samples is markedly different from the Plinian samples. Similar to experimentally deformed samples, they have measurable permeabilities down to small values of ϕ_t, consistent with their high connectivity (Figure 11). As in the experiments of Okumura et al. (2009) we observe bubble elongation and alignment in our deformed samples (Figure 10). Although it is likely that our deformed samples are anisotropic with respect to permeability, we do not quantify this. Instead we characterize permeability in the direction perpendicular to the shear plane, which presumably is a close approximation of the transverse component of the permeability tensor. Overall, our experiments substantiate the hypothesis that compacting magma will remain permeable down to low porosities (Table A3). Permeability may be reduced as the size of pores and pore apertures are reduced (Blower, 2001a; Rust & Cashman, 2004), but pore connectivity persists for the most part. In the presence of shear there could also be an increase in connectivity, as indicated by some of the experiments (Figures 8b and 8d).

Percolation modeling cannot produce the high values of connectivity measured for experimentally deformed samples or for effusively erupted natural samples (Figure 11b). Even at $\varepsilon = 0$ connected porosity is significantly smaller in percolation models (Figure 5a) than measured in the deformed Glass Mountain samples (Figure 9b). Although not modeled here, higher connectivity can only be achieved in percolation models if bubbles are allowed to have nonspherical shapes (Garboczi et al., 1995; Yi & Sastry, 2004). This is consistent with the interpretation that bubble elongation accounts to some extent for permeability in compacted samples.

7. Conclusions

All explosively erupted samples considered herein are permeable and span porosities of approximately 0.6–0.9. Permeabilities can be fitted by power law with a porosity threshold of ≥0.6, potentially consistent with thresholds observed in vesiculation experiments. Because of the lack of impermeable samples a lower threshold can, however, not be ruled out. The lack of low-porosity explosive samples, which has been interpreted to indicate that impermeable magma fragments to ash size (Rust & Cashman, 2011) could also indicate that the entire magma was permeable when it reached fragmentation conditions. Effusively erupted samples and experimentally compacted samples remain permeable down to low porosities. They show a high degree of pore connectivity, regardless of porosity, suggesting that pore apertures, due to coalesced bubbles, remain intact as magma compacts, albeit at reduced size. Shear deformation elongates and aligns bubbles, and our results support the hypothesis that shear deformation enhances coalescence. Results are consistent with the hypothesis that the effusive eruption of low-porosity silicic magma is facilitated by magma remaining permeable down to very low porosities. To first order, the change in permeability during compaction can be described by an equation that accounts for decreasing bubble size, but future improvements could address apparent changes in connectivity and permeability associated with shear deformation and capillary stresses.

Appendix A: Data Tables

Tables listing porosity and permeability measurements for the Glass Mountain Plinian samples (Table A1), as well as deformation data for the Glass Mountain Plinian samples (Table A2) and resultant porosity and permeability (Table A3) are presented. In addition, tables listing newly measured porosities and permeabilities for Taupo Plinian fall samples (Table A4), El Cajete Plinian fall samples (Table A5), Long Valley (Bishop Tuff) samples (Table A6), and Glass Mountain lava flow samples (Table A7) are presented.

Table A1
Porosity-Permeability Data for Glass Mountain Samples

Sample ID	L (mm)	D (mm)	ϕ_t (%)	ϕ_c (%)	C (%)	$\log_{10}k$ (m^2)	$\log_{10}k^*$ (m)
BGM2-1	13.22	19.91	78.33	75.70	96.64	−11.23	−7.55
BGM2-2	14.64	19.47	81.27	79.48	97.80	−11.56	−7.91
BGM4-1	15.89	19.24	80.33	70.19	87.38	−11.71	−8.00
BGM4-2	14.15	18.80	80.16	73.61	91.83	−10.93	−6.49
BGM4-4	16.83	18.81	82.66	77.49	93.75	−10.77	−5.81
BGM4-5	14.51	19.48	83.69	73.12	87.36	−11.86	−9.47
BGM5-1	24.55	19.79	75.34	72.11	95.71	−12.54	−8.60
BGM5-2	21.14	19.67	75.73	73.76	97.39	−13.07	−9.52
BGM6-1	17.82	19.78	73.84	64.77	87.72	−12.06	−7.98
BGM6-2	17.15	19.67	79.43	71.06	89.46	−11.14	−7.10
BGM6-3	16.20	19.70	72.43	61.84	85.38	−12.30	−8.25
BGM6-4	17.03	19.77	73.83	64.10	86.83	−11.86	−7.71
BGM6-5	16.17	19.73	71.66	61.15	85.33	−12.06	−7.93
BGM6-6	17.11	19.79	78.28	71.25	91.02	−12.34	−8.34
BGM6-7	13.96	19.65	73.05	62.15	85.07	−13.10	−9.65
BGM6-8	10.79	19.72	73.20	63.39	86.61	−12.74	−9.02
BGM6-9	15.33	19.79	80.84	75.30	93.15	−11.34	−7.03
BGM8-2	16.40	19.30	84.80	82.99	97.86	−10.77	−5.85
BGM8-3	24.41	19.56	73.98	69.18	93.51	−13.87	−10.33
BGM8-4	22.67	19.63	81.54	77.21	94.69	−12.30	−9.11
BGM8-5	18.50	19.57	78.71	74.72	94.92	−12.98	−9.11
BGM8-6	18.59	19.16	77.10	69.59	90.25	−11.14	−7.62
BGM8-7	25.52	19.37	78.65	73.02	92.85	−12.62	−9.29
BGM8-8	14.97	19.49	73.33	64.27	87.64	−13.27	−9.97
BGM8-9	18.10	19.65	76.30	69.67	91.31	−12.78	−9.47
BGM20-1	16.60	19.76	72.22	61.83	85.61	−13.31	−9.42
BGM20-3	14.61	19.77	75.51	66.75	88.39	−13.19	−9.56
BGM20-4	22.08	19.93	75.34	65.41	86.83	−10.89	−7.07
BGM21-1	15.61	19.27	78.89	73.26	92.87	−10.93	−6.40
BGM21-2	17.18	19.60	78.12	70.66	90.45	−11.89	−7.69
BGM21-3	17.22	19.36	80.36	79.82	99.32	−10.60	−6.53
BGM21-4	18.08	19.84	75.22	65.14	86.61	−12.50	−8.75
BGM22-1	14.24	19.64	71.29	66.18	92.84	−12.79	−8.51
BGM22-2	13.82	19.59	71.10	62.94	88.53	−12.35	−8.45
BGM22-3	24.69	19.82	75.04	69.43	92.53	−12.82	−9.43
BGM22-5	13.10	19.71	68.19	59.65	87.48	−13.99	−10.38
BGM22-6	18.70	19.86	74.33	69.28	93.21	−13.01	−9.38
BGM23-2	16.14	18.99	79.08	77.61	98.15	−10.96	−6.19
BGM23-3	16.92	19.83	72.06	67.65	93.88	−11.92	−6.91
BGM24-1	15.36	19.17	77.20	74.26	96.19	−11.02	−6.58
BGM24-2	12.99	19.32	76.28	73.10	95.83	−11.84	−7.27
BGM24-3	25.00	19.48	78.21	72.80	93.09	−13.58	−9.71

Table A1 *(continued)*

Smple ID	L (mm)	D (mm)	ϕ_t (%)	ϕ_c (%)	C (%)	$\log_{10} k$ (m^2)	$\log_{10} k^*$ (m)
BGM24-4	24.06	19.82	72.72	68.49	94.19	−11.98	−7.15
BGM34-1	19.82	19.64	86.52	85.98	99.38	−11.98	−8.12
BGM34-2	20.91	19.71	84.63	83.56	98.74	−12.37	−8.41
BGM37-1	19.62	19.85	78.19	73.95	94.57	−13.34	−9.62
BGM37-2	20.25	19.86	78.43	73.94	94.27	−13.22	−9.65
BGM-P-A2a-1	21.29	19.99	76.67	68.99	89.98	−13.06	−9.78
BGM-P-A2a-2	14.90	19.96	75.35	67.44	89.50	−13.11	−9.92
BGM-P-A2a-3	22.72	19.97	73.72	65.72	89.15	−13.89	−10.80
BGM-P-A2a-4	18.59	19.02	69.79	59.6	85.40	−14.91	−12.05
BGM-P-A2a-5	19.43	20.00	72.52	63.77	87.94	−14.51	−11.91
BGM-P-A2c	12.68	19.91	69.10	56.12	81.21	−13.19	−9.70
BGM-P-A2e-1	19.42	19.45	76.68	69.97	91.25	−13.39	−9.82
BGM-P-A2e-2	15.54	19.47	80.35	74.6	92.85	−11.73	−8.21
BGM-P-A2e-3	20.76	19.83	75.80	69.02	91.06	−13.21	−9.92
BGM-P-A2g-1	16.77	19.92	75.47	63.99	84.79	−12.92	−9.44
BGM-P-A2g-2	15.25	19.92	80.69	70.17	86.96	−12.81	−9.45
BGM-P-A2g-3	18.84	19.69	83.69	77.37	92.45	−12.12	−8.57

Table A2
Porosity-Permeability Data for Deformed Samples

ID	$\phi_t^{[i]}$	$\phi_c^{[i]}$	$\phi_t^{[f]}$	$\phi_c^{[f]}$	$\log_{10} k^{[i]}$ (m^2)	$\log_{10} k^{[f]}$ (m^2)	$(\log_{10} k^*)^{[i]}$ (m)	$(\log_{10} k^*)^{[f]}$ (m)	γ (mrad)	ε (%)
BGM5-2	75.73	73.76	47.11	43.85	−13.07	−13.55	−9.52	−10.29	1583	−45.82
BGM6-2	79.43	71.06	74.13	70.7	−11.14	−10.51	−7.10	−6.50	312	−11.10
BGM6-6	78.28	71.25	71.25	66.04	−12.34	−12.27	−8.34	−8.11	669	−23.00
BGM6-8	73.2	63.39	40.73	36.79	−12.74	−14.44	−9.02	−10.87	1532	−43.96
BGM8-3	73.98	69.18	61.90	58.83	−13.87	−14.12	−10.33	−10.66	580	−23.97
BGM8-5	78.71	74.72	66.88	64.75	−12.98	−12.39	−9.11	−8.27	582	−19.02
BGM8-8	73.33	64.27	64.34	60.33	−13.27	−12.29	−9.97	−8.81	329	−11.07
BGM20-1	72.22	61.83	22.21	15.87	−13.31	−15.34	−9.42	−14.59	2155	−50.36
BGM20-2	76.68	67.96	32.01	26.69	−13.25	−14.98	−9.49	−12.27	2010	−54.93
BGM20-3	75.51	66.75	50.55	46.49	−13.19	−13.85	−9.56	−10.04	972	−34.41
BGM24-3a	78.21	72.80	71.28	69.14	−13.58	−13.27	−9.71	−9.79	380	−18.31
BGM24-3b	78.21	72.80	62.49	59.80	−13.58	−12.93	−9.71	−9.49	824	−36.89
BGM-P-A2a-5	72.52	63.77	40.25	32.15	−14.51	−14.78	−11.91	−11.82	1266	−37.89
BGM-P-A2e-1	76.68	69.97	58.22	54.67	−13.06	−13.69	−9.78	−10.07	943	−32.11
BGM-P-A2m-3	79.56	71.26	33.09	25.79	−11.94	−14.64	−8.15	−11.22	1804	−51.22
BGM-P-1B-1	69.53	59.37	42.42	40.01	−12.88	−14.00	−9.16	−10.28	1085	−36.94
BGM-P-3C-1	71.97	67.15	47.81	45.67	−12.66	−13.67	−8.93	−9.97	1170	−43.67

Note. Superscript [i] denotes value prior to deformation. Superscript [f] denotes value after deformation.

Table A3
Deformation Data

ID	$\log_{10} \dot{\gamma}^{[i]}$ (s^{-1})	$\log_{10} \dot{\gamma}^{[f]}$ (s^{-1})	$R^{[i]}$ (mm)	$R^{[f]}$ (mm)	$L^{[i]}$ (mm)	$L^{[f]}$ (mm)	σ (N)
BGM5-2	−3.18	−4.05	7.05	6.48	9.69	5.25	2
BGM6-2	−2.91	−3.04	7.30	6.87	7.12	6.33	2
BGM6-6	−3.59	−4.64	7.50	7.15	11.00	8.47	2
BGM6-8	−3.04	−3.93	7.25	6.36	7.78	4.36	2
BGM8-3	−3.08	−3.46	7.36	6.8	8.22	6.25	2

Table A3 *(continued)*

ID	$\log_{10} \dot{\gamma}^{[i]}$ (s⁻¹)	$\log_{10} \dot{\gamma}^{[f]}$ (s⁻¹)	$R^{[i]}$ (mm)	$R^{[f]}$ (mm)	$L^{[i]}$ (mm)	$L^{[f]}$ (mm)	σ (N)
BGM8-5	−3.30	−3.70	7.51	7.03	6.1	4.94	2
BGM8-8	−3.19	−4.10	7.49	6.99	9.58	4.35	2
BGM20-1	−3.28	−4.20	7.48	6.67	9.71	4.82	2
BGM20-2	−3.27	−3.50	7.54	6.69	8.22	7.31	2
BGM20-3	−3.20	−3.73	7.35	6.54	8.37	5.49	2
BGM24-3a	−3.03	−3.16	7.27	6.79	7.32	5.98	2
BGM24-3b	−2.74	−3.26	7.35	6.84	7.40	4.67	2
BGM-P-A2a-5	−3.23	−3.95	7.17	6.28	8.63	5.36	2
BGM-P-A2e-1	−3.01	−3.49	6.88	6.28	8.75	5.94	2
BGM-P-A2m-3	−3.11	−3.96	6.95	5.99	9.43	4.60	2
BGM-P-1B-1	−3.15	−4.12	7.35	6.70	8.77	5.53	2
BGM-P-3C-1	−3.12	−3.81	7.3	6.57	9.55	5.38	2

Note. Superscript [i] denotes value prior to deformation.   Superscript [f] denotes value after deformation.

Table A4
Porosity-Permeability Data for Taupo Plinian Fall

ID	L (mm)	D (mm)	ϕ_t (%)	ϕ_c (%)	C	$\log_{10} k$ (m²)	$\log_{10} k^*$ (m)
TP-06-01	15.00	9.10	74.07	67.87	0.92	−13.62	−9.55
TP-21-11	20.03	9.04	74.02	67.79	0.92	−13.78	−9.72
TP-189-03	18.54	9.10	73.72	67.19	0.91	−13.49	−9.37
TP-18C-01-1	17.70	9.04	79.17	74.23	0.94	−13.51	−9.70
TP-18C-01-2	12.36	8.94	78.95	74.04	0.94	−13.72	−9.80
TP-18A-01	17.19	9.13	72.89	68.02	0.93	−13.89	−9.99
TP-18b-04-1	21.08	7.10	70.18	64.99	0.93	−13.91	−10.27
TP-18b-04-2	13.33	9.03	72.97	68.24	0.94	−13.59	−9.72
TP-18C-25	20.14	9.02	77.58	71.62	0.92	−13.17	−9.00
TP-17a-11	13.67	7.16	76.38	72.55	0.95	−13.83	−10.03
TP-18b-03-1	12.65	7.20	73.85	69.68	0.94	−13.93	−10.24
TP-18b-03-2	8.49	6.46	76.03	74.00	0.97	−13.67	−9.80
TP-16-04	28.00	9.18	79.42	71.84	0.90	−13.07	−8.92
TR09A-02	21.23	9.06	75.52	70.12	0.93	−13.67	−9.67
TP-07-10	17.01	7.08	74.67	73.08	0.98	−14.05	−10.66
TP-07-07	14.82	7.22	76.31	73.02	0.96	−12.94	−8.34
TP-21-04	14.96	9.20	73.37	57.64	0.79	−13.18	−8.81
TP-13a-03	14.66	9.07	76.95	71.00	0.92	−13.66	−9.74
TP-13b-04	19.04	9.02	76.58	69.64	0.91	−13.40	−9.35
TP-14-06	15.78	7.13	75.61	70.01	0.93	−14.02	−10.27
TP-15b-05	15.89	9.11	75.80	72.66	0.96	−13.51	−9.51
TP-15A-01-1	15.93	9.12	76.71	69.86	0.91	−13.77	−9.87

Table A5
Porosity-Permeability Data for El Cajete Plinian Fall

ID	L (mm)	D (mm)	ϕ_t (%)	ϕ_c (%)	C	$\log_{10} k$ (m²)	$\log_{10} k^*$ (m)
VC3-1	−16.31	18.99	81.47	78.59	0.96	−11.54	−7.12
VC3-2	16.62	18.96	81.52	78.43	0.96	−11.46	−6.94
VC4	15.21	19.19	83.4	83.19	0.99	−11.22	−6.04
VC5	14.78	19.67	73.11	67.87	0.93	−12.38	−7.98

Table A5 (continued)

| ID	L (mm)	D (mm)	ϕ_t (%)	ϕ_c (%)	C	$\log_{10} k$ (m^2)	$\log_{10} k^*$ (m)
VC7	15.51	19.75	73.97	69.35	0.94	−12.26	−7.84
VC8-1	16.49	19.84	77.76	75.08	0.97	−12.34	−8.57
VC8-3	24.22	19.84	76.62	74.70	0.97	−12.42	−8.43
VC8-4	16.83	19.84	75.28	73.11	0.97	−11.77	−7.91
VC8-5	24.56	19.84	79.50	78.04	0.98	−11.54	−7.93
VC8-6	22.80	19.86	78.50	76.44	0.97	−11.62	−7.48
VC9-1	16.04	19.81	78.88	75.85	0.96	−12.14	−8.12
VC9-2	22.44	19.96	78.84	75.27	0.95	−11.42	−6.71
VC10-2	14.84	18.67	83.31	81.23	0.98	−11.53	−7.23
VC10-3	18.92	19.72	83.27	80.98	0.97	−11.19	−6.71

Table A6
Porosity-Permeability Data for Long Valley Samples

ID	L (mm)	D (mm)	ϕ_t (%)	ϕ_c (%)	C	$\log_{10} k$ (m^2)	$\log_{10} k^*$ (m)
LV-BT-P-1-1	16.65	19.84	70.69	61.34	86.77	−12.26	−8.16
LV-BT-P-1-2	15.13	19.86	69.75	68.65	98.42	−13.06	−9.29
LV-BT-P-1-3	17.84	19.83	71.72	63.51	88.55	−12.72	−8.92
LV-BT-P-1-5	20.23	19.57	70.25	69.52	98.97	−13.11	−9.38
LV-BT-P-1-6	15.64	19.82	70.80	69.30	97.89	−13.01	−9.37
LV-BT-P-1-7	18.24	19.64	70.85	68.87	97.21	−13.51	−9.74
LV-BT-P-1-8	21.89	19.80	71.67	69.83	97.43	−12.22	−8.70
LV-BT-P-2-1	16.17	19.95	65.13	58.31	89.53	−11.54	−7.62
LV-BT-P-2-2	16.14	20.03	64.10	56.01	87.38	−11.66	−7.75
LV-BT-P-3-1	16.07	19.90	74.45	71.10	95.51	−12.34	−8.84
LV-BT-P-3-2	13.08	19.86	74.20	70.36	94.82	−12.42	−8.61
LV-BT-P-4-1	15.22	20.02	67.54	64.59	95.63	−13.42	−9.47
LV-BT-P-4-2	12.18	19.82	69.27	67.01	96.74	−11.70	−8.21
LV-BT-P-5-1	15.02	19.85	70.90	68.44	96.53	−12.46	−8.75
LV-BT-P-5-2	12.46	19.95	73.60	70.59	95.91	−12.38	−8.66
LV-BT-P-6	17.78	19.92	66.88	62.70	93.75	−12.34	−8.25
LV-BT-P-7-1	15.56	19.95	68.29	62.79	91.95	−13.23	−9.88
LV-BT-P-7-2	16.78	19.89	67.65	61.94	91.57	−13.43	−10.15
LV-BT-P-8	14.07	19.89	68.21	62.61	91.79	−11.86	−8.12
LV-BT-P-9	13.66	20.00	63.69	56.31	88.41	−14.15	−10.92
LV-PC-10-1	15.36	19.92	71.92	71.39	99.26	−12.14	−7.62
LV-PC-10-2	19.47	19.70	71.90	71.15	98.96	−12.18	−7.62
LV-PC-10-3	19.70	19.90	72.55	70.95	97.80	−12.06	−7.53
LV-PC-10-4	20.14	19.88	72.83	71.58	98.28	−11.46	−6.40
LV-PC-11-1	19.18	19.91	66.29	63.97	96.51	−11.94	−7.84
LV-PC-11-2	12.49	19.88	67.37	65.48	97.19	−11.30	−7.26
LV-PC-11-3	18.53	19.90	66.64	64.52	96.83	−11.70	−7.62
LV-PC-11-4	20.53	19.87	66.24	63.87	96.42	−12.02	−8.03
LV-PC-12-1	23.29	19.80	65.45	62.65	95.72	−12.98	−9.29
LV-PC-12-2	19.47	19.89	65.66	63.36	96.50	−13.07	−9.25
LV-PC-12-3	16.61	19.93	66.52	63.72	95.78	−13.07	−9.47
LV-PC-14-3	19.73	19.51	73.92	74.23	100.41	−11.22	−6.29

Table A7
Porosity-Permeability Data for Glass Mountain Lava Flow

ID	L (mm)	D (mm)	ϕ_t (%)	ϕ_c (%)	C	$\log_{10} k$ (m^2)	$\log_{10} k^*$ (m)
BGM11-1	17.90	19.86	60.03	58.49	97.43	−10.81	−5.58
BGM11-3	16.54	19.92	57.86	56.35	97.39	−11.22	−7.08
BGM11-4	16.39	19.80	66.48	65.66	98.77	−10.81	−4.77
BGM11-5	22.43	19.60	57.58	55.22	95.90	−11.18	−6.89
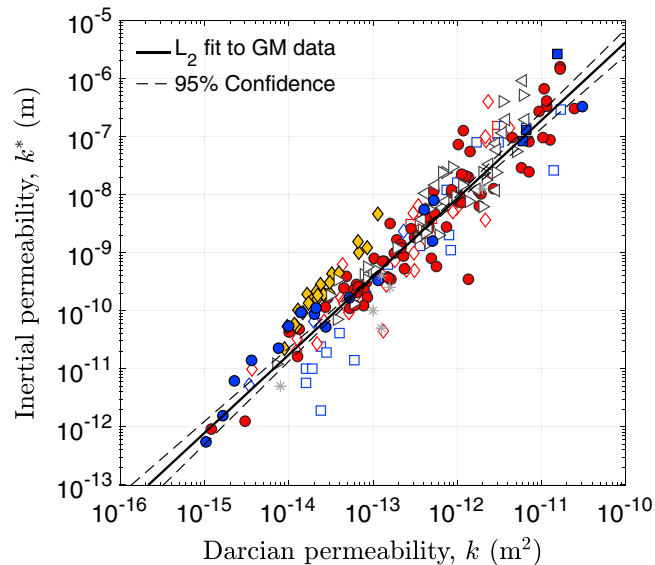
Figure B1. Inertial (non-Darcian) permeability, k^*, as a function of Darcian permeability, k. Lines are least squares fit according to equation (B1).

Appendix B: Darcian and Inertial Permeabilities

A well-defined functional relation between Darcian permeability, k, and inertial permeability, k^*, exists for all samples (Figure B1). Shown in Figure B1 is the least squares linear fit based solely on the Glass Mountain Plinian and deformed samples, together with 95% confidence intervals. The fit is given by

$$\log_{10}(k^*) = 1.353\,(\pm 0.088) \times \log_{10}(k) + 8.175\,(\pm 2.237) \tag{B1}$$

and results in a root-mean-square error in $\log_{10}(k^*)$ of 0.4466. The fit is similar to the broad relationship found for other volcanic samples, and we refer, for example, to Burgisser et al. (2017, and references therein) for a more in-depth discussion.

Notation

Vesicularity Determination

$$C = \phi_c/\phi_t \quad = \text{Vesicle connectivity;}$$
$$L \quad = \text{Sample length;}$$
$$M_t \quad = \text{Mass;}$$
$$R \quad = \text{Sample radius;}$$
$$V_c = V_t - V_s \quad = \text{Connected volume of vesicles within sample;}$$
$$V_m = M_t/\rho_m \quad = \text{Volume of solid matrix;}$$
$$V_s \quad = \text{Skeletal volume;}$$
$$V_t \quad = \text{Envelope volume;}$$
$$\rho_m \quad = \text{Average matrix density from } V_m \text{ and mass of crushed sample;}$$

$\phi_c = V_c/V_t$ = Connected porosity;

$\phi_t = (V_t - V_m)/V_t$ = Total porosity.

Permeability determination

k = Darcian permeability coefficient (equation (1));

k^* = Non-Darcian permeability coefficient (equation (1));

q = Flow rate of air during permeability measurement;

N = Number of measurement points per permeability measurement;

P_1 = Inlet pressure during flow rate measurement;

P_2 = Outlet pressure during flow rate measurement;

η_g = Viscosity of air.

Analysis

$a = b \cdot r^2$ = Constant;

b = Fitting parameter (equation (2));

n = Fitting parameter (equations (2)) and equation (11);

r = Average vesicle radius obtained from analysis of SEM images;

α = Fitting parameter (equation (1));

β = Fitting parameter (equation (4));

ϵ = Measured axial strain during sample deformation;

ϵ = Geometrical parameter in percolation model;

γ = Shear stress during sample deformation (equation (7));

$\dot{\gamma}$ = Shear rate during sample deformation;

λ = Fitting parameter (equation (4));

θ = Measured deflection angle during sample deformation;

σ = Applied normal force during sample deformation;

τ = Shear stress during sample deformation (equation (8));

ϕ_{cr} = Estimated percolation threshold;

Γ = Applied torque during sample deformation;

Ω = Rotation rate during sample deformation.

References

Adams, N. K., Houghton, B. F., Fagents, S. A., & Hildreth, W. (2006). The transition from explosive to effusive eruptive regime: The example of the 1912 Novarupta eruption, Alaska. *Geological Society of America Bulletin*, *118*, 620–634. https://doi.org/10.1130/B25768.1

Adams, N. K., Houghton, B. F., & Hildreth, W. (2006). Abrupt transitions during sustained explosive eruptions: Examples from the 1912 eruption of Novarupta, Alaska. *Bulletin of Volcanology*, *69*, 189–206. https://doi.org/10.1007/s00445-006-0067-4

Anderson, C. A. (1933). Volcanic history of glass mountain, Northern California. *American Journal of Science*, *5*, 485–4506.

Ashwell, P. A., Kendrick, J. E., Lavallée, Y., Kennedy, B. M., Hess, K.-U., von Aulock, F. W., … Dingwell, D. B. (2015). Permeability of compacting porous lavas. *Journal of Geophysical Research: Solid Earth*, *120*, 1605–1622. https://doi.org/10.1002/2014JB011519

Bagdassarov, N. S., & Dingwell, D. B. (1992). A rheological investigation of vesicular rhyolite. *Journal of Volcanology and Geothermal Research*, *50*, 307–322. https://doi.org/10.1016/0377-0273(92)90099-Y

Bagdassarov, N. S., & Dingwell, D. B. (1994). Thermal properties of vesicular rhyolite. *Journal of Volcanology and Geothermal Research*, *60*, 179–191. https://doi.org/10.1016/0377-0273(94)90067-1

Berryman, J. G., & Blair, S. C. (1987). Kozeny Carmen relations and image processing methods for estimating Darcy's constant. *Journal of Applied Physics*, *62*, 2221–2228. https://doi.org/10.1063/1.339497

Blower, J. D. (2001a). A three-dimensional network model of permeability invesicular material. *Computers and Geosciences*, *27*, 115–110. https://doi.org/10.1016/S0098-3004(00)00066-2

Blower, J. D. (2001b). Factors controlling permeability-porosity relationships in magma. *Bulletin of Volcanology*, *63*, 497–504. https://doi.org/10.1007/s004450100172

Burgisser, A., & Gardner, J. E. (2005). Experimental constraints on degassing and permeability in volcanic conduit flow. *Bulletin of Volcanology*, *67*, 42–56. https://doi.org/10.1007/s00445-004-0359-5

Burgisser, A., Chevalier, L., Gardner, J. E., & Castro, J. M. (2017). The percolation threshold and permeability evolution of ascending magmas. *Earth and Planetary Science Letters*, *470*, 37–47. https://doi.org/10.1016/j.epsl.2017.04.023

Cashman, K. V., & Mangan, M. T. (1994). Physical aspects of magmatic degassing II. constraints on vesiculation processes from textural studies of eruptive products. In M. R. Carroll & J. R. Holloway (Eds.), *Volatiles in magmas, Reviews in Mineralogy* (Vol. 30, pp. 447–478). Washington, DC: Mineralogical Society of America.

Cashman, K. V., & Scheu, B. (2015). Magmatic fragmentation (2nd edn). In H. Sigurdsson, et al. (Eds.), *The encyclopedia of volcanoes* (pp. 459–472). San Diego, CA: Academic Press.

Castro, J. M., Bindeman, I. N., Tuffen, H., & Schipper, C. I. (2014). Explosive origin of silicic lava: Textural and $\delta D–H_2O$ evidence for pyroclastic degassing during rhyolite effusion. *Earth and Planetary Science Letters*, *405*, 52–61. https://doi.org/10.1016/j.epsl.2014.08.012

Castro, J. M., Burgisser, A., Schipper, C. I., & Mancini, S. (2012). Mechanisms of bubble coalescence in silicic magmas. *Bulletin of Volcanology*, *74*, 2339–2352. https://doi.org/10.1007/s00445-012-0666-1

Castro, J. M., Cordonnier, B., Tuffen, H., Tobin, M. J., Puskar, L., Martin, M. C., & Bechtel, H. A. (2012). The role of melt-fracture degassing in defusing explosive rhyolite eruptions at volcán Chaitén. *Earth and Planetary Science Letters*, *333–334*, 63–69. https://doi.org/10.1016/j.epsl.2012.04.024

Castro, J. M., Schipper, C. I., Mueller, S. P., Militzer, A. S., Amigo, A., Parejas, C. S., & Jacob, D. (2013). Storage and eruption of near-liquidus rhyolite magma at Cordón Caulle, Chile. *Bulletin of Volcanology*, *75*, 702–719. https://doi.org/10.1007/s00445-013-0702-9

Chiarabba, C., Amato, A., & Evans, J. R. (2012). Variations on the NeHT high-resolution tomography method: A test of technique and results for Medicine Lake Volcano, northern California. *Journal of Geophysical Research*, *100*, 4035–4052. https://doi.org/10.1029/94JB02771

Colombier, M., Wadsworth, F. B., Gurioli, L., Scheu, B., Kueppers, U., Di Muro, A., & Dingwell, D. B. (2017). The evolution of pore connectivity in volcanic rocks. *Earth and Planetary Science Letters*, *462*, 99–109. https://doi.org/10.1016/j.epsl.2017.01.011

Degruyter, W., Bachmann, O., Burgisser, A., & Manga, M. (2012). The effects of outgassing on the transition between effusive and explosive silicic eruptions. *Earth and Planetary Science Letters*, *349–350*, 161–170. https://doi.org/10.1016/j.epsl.2012.06.056

Donnelly-Nolan, J. M., Champion, D. E., Miller, C. D., Grove, T. L., & Trimble, D. A. (1990). Post-11,000-year volcanism at Medicine Lake Volcano, Cascade Range, northern California. *Journal of Geophysical Research*, *95*, 19,693–19,704. https://doi.org/10.1029/JB095iB12p19693

Donnelly-Nolan, J. M., Nathenson, M., Chammpion, D. E., Ramsey, D. W., Lowenstern, J. B., & Ewert, J. W. (2007). Volcano hazards assessment for Medicine Lake Volcano, Northern California (Technical Report 2007-5174-A). Reston, VA: U.S. Department of the Interior, U.S. Geological Survey.

Donnelly-Nolan, J. M., Grove, T. L., Lanphere, M. A., Champion, D. E., & Ramsey, D. W. (2008). Eruptive history and tectonic setting of Medicine Lake Volcano, a large rear-arc volcano in the southern Cascades. *Journal of Volcanology and Geothermal Research*, *177*, 313–328. https://doi.org/10.1016/j.jvolgeores.2008.04.023

Eichelberger, J. C., Carrigan, C. R., Westrich, H. R., & Price, R. H. (1986). Non-explosive silicic volcanism. *Nature*, *323*, 598–602.

Evans, J. R., & Zucca, J. J. (2012). Active high-resolution seismic tomography of compressional wave velocity and attenuation structure at Medicine Lake Volcano, Northern California Cascade Range. *Journal of Geophysical Research*, *93*, 15,016–15,036. https://doi.org/10.1029/JB093iB12p15016

Farquharson, J. I., Heap, M. J., Lavaée, Y., Varley, N. R., & Baud, P. (2016). Evidence for the development of permeability anisotropy in lava domes and volcanic conduits. *Journal of Volcanology and Geothermal Research*, *323*, 163–185. https://doi.org/10.1016/j.jvolgeores.2016.05.007

Farquharson, J. I., Wadsworth, F. B., Heap, M. J., & Baud, P. (2017). Time-dependent permeability evolution in compacting volcanic fracture systems and implications for gas overpressure. *Journal of Volcanology and Geothermal Research*, *339*, 81–97. https://doi.org/10.1016/j.jvolgeores.2017.04.025

Fierstein, J., & Hildreth, W. (1992). The plinian eruptions of 1912 at Novarupta, Katmai National Park, Alaska. *Bulletin of Volcanology*, *54*, 646–684. https://doi.org/10.1007/BF00430778

Forchheimer, P. (1901). Wasserbewegung durch Boden. *Zeitschrift des Vereins Deutscher Ingenieure*, *45*, 1781–1788.

Garboczi, E. J., Snyder, K. A., Douglas, J. F., & Thorpe, M. F. (1995). Geometrical percolation threshold of overlapping ellipsoids. *Physical Review E: Covering Statistical, Nonlinear, Biological, and Soft Matter Physics*, *52*, 819–828. https://doi.org/10.1103/PhysRevE.52.819

Gardner, J., Carey, S., & Sigurdsson, H. (1998). Plinian eruptions at Glacier Peak and Newberry volcanoes, United States: Implications for volcanic hazards in the Cascade Range. *Geological Society of America Bulletin*, *110*, 173–187. https://doi.org/10.1130/0016-7606(1998)110<0173:PEAGPA>2.3.CO;2

Gardner, J. E., Sigurdsson, H., & Carey, S. N. (1991). Eruption dynamics and magma withdrawal during the Plinian Phase of the Bishop Tuff Eruption, Long Valley Caldera. *Journal of Geophysical Research*, *96*, 8097–8111. https://doi.org/10.1029/91JB00257

Giachetti, T., Burgisser, A., Arbaret, L., Druitt, T. H., & Kelfoun, K. (2011). Quantitative textural analysis of Vulcanian pyroclasts (Montserrat) using multi-scale X-ray computed microtomography: Compared with results from 2D image analysis. *Bulletin of Volcanology*, *73*, 1295–1309. https://doi.org/10.1007/s00445-011-0472-1

Giachetti, T., Druitt, T., Burgisser, A., Arbaret, L., & Galven, C. (2010). Bubble nucleation, growth and coalescence during the 1997 Vulcanian explosions of Soufrière Hills Volcano, Montserrat. *Journal of Volcanology and Geothermal Research*, *193*, 215–231. https://doi.org/10.1016/j.jvolgeores.2010.04.001

Giachetti, T., & Gonnermann, H. M. (2013). Water in volcanic pyroclasts rehydration or incomplete degassing? *Earth and Planetary Science Letters*, *369–370*, 317–332. https://doi.org/10.1016/j.epsl.2013.03.041

Giachetti, T., Gonnermann, H. M., Gardner, J. E., Shea, T., & Gouldstone, A. (2015). Discriminating secondary from magmatic water in rhyolitic matrix-glass of volcanic pyroclasts using thermogravimetric analysis. *Geochimica et Cosmochimica Acta*, *148*, 457–476. https://doi.org/10.1016/j.gca.2014.10.017

Gonnermann, H. M. (2015). Magma fragmentation. *Annual Review of Earth and Planetary Sciences*, *43*, 431–458. https://doi.org/10.1146/annurev-earth-060614-105206

Gonnermann, H. M., & Manga, M. (2003). Explosive volcanism may not be an inevitable consequence of magma fragmentation. *Nature*, *426*, 432–435. https://doi.org/10.1038/nature02138

Gonnermann, H. M., & Manga, M. (2005). Flow banding in obsidian: A record of evolving textural heterogeneity during magma fragmentation. *Earth and Planetary Science Letters*, *236*, 135–147. https://doi.org/10.1016/j.epsl.2005.04.031

Gonnermann, H. M., & Manga, M. (2007). The fluid mechanics inside a volcano. *Annual Review of Fluid Mechanics*, *39*, 321–356. https://doi.org/10.1146/annurev.fluid.39.050905.110207

Grove, T. L., & Donnelly-Nolan, J. M. (1986). The evolution of young silicic lavas at Medicine Lake Volcano, California: Implications for the origin of compositional gaps in calc-alkaline series lavas. *Contributions to Mineralogy and Petrology*, *92*, 281–302.

Grove, T. L., Donnelly-Nolan, J. M., & Housh, T. (1997). Magmatic processes that generated the rhyolite of Glass Mountain, Medicine Lake volcano, north California. *Contributions to Mineralogy and Petrology*, *127*, 205–223.

Heap, M. J., & Kennedy, B. M. (2016). Exploring the scale-dependent permeability of fractured andesite. *Earth and Planetary Science Letters*, *447*, 139–150. https://doi.org/10.1016/j.epsl.2016.05.004

Heap, M. J., Violay, M., Wadsworth, F. B., & Vasseur, J. (2017). From rock to magma and back again: The evolution of temperature and deformation mechanism in conduit margin zones. *Earth and Planetary Science Letters*, *463*, 92–100. https://doi.org/10.1016/j.epsl.2017.01.021

Heiken, G. (1978). Plinian-type eruptions in the Medicine Lake Highland, California, and the nature of the underlying magma. *Journal of Volcanology and Geothermal Research*, *4*, 375–402. https://doi.org/10.1016/0377-0273(78)90023-9

Hildreth, E. W., & Fierstein, J. (2012). The Novarupta-Katmai eruption of 1912—Largest eruption of the twentieth century: Centennial perspectives (259 p.).

Hildreth, W., & Fierstein, J. (2000). Katmai volcanic cluster and the great eruption of 1912. *Geological Society of America Bulletin*, *112*, 1594–1620. https://doi.org/10.1130/0016-7606(2000)112<1594:KVCATG>2.0.CO;2

Hildreth, W., & Wilson, C. J. (2007). Compositional zoning of the Bishop Tuff. *Journal of Petrology*, *48*, 951–999. https://doi.org/10.1093/petrology/egm007

Houghton, B. F., Carey, R. J., Cashman, K. V., Wilson, C., Hobden, B. J., & Hammer, J. E. (2010). Diverse patterns of ascent, degassing, and eruption of rhyolite magma during the 1.8 ka Taupo eruption, New Zealand: Evidence from clast vesicularity. *Journal of Volcanology and Geothermal Research*, *195*, 31–47. https://doi.org/10.1016/j.jvolgeores.2010.06.002

Houghton, B. F., Carey, R. J., & Rosenberg, M. (2014). The 1800a Taupo eruption: "Ill wind" blows the ultraplinian type event down to Plinian. *Geology*, *42*, 459–461. https://doi.org/10.1130/G35400.1

Houghton, B. F., & Wilson, C. J. N. (1989). A vesicularity index for pyroclastic deposits. *Bulletin of Volcanology*, *51*, 451–462. https://doi.org/10.1007/BF01078811

Jaupart, C., & Allègre, C. J. (1991). Gas content, eruption rate and instabilities of eruption regime in silicic volcanos. *Earth and Planetary Science Letters*, *102*, 413–429. https://doi.org/10.1016/0012-821X(91)90032-D

Kennedy, B. M., Wadsworth, F. B., Vasseur, J., Schipper, C. I., Jellinek, A. M., von Aulock, F. W., . . . Dingwell, D. B. (2016). Surface tension driven processes density and retain permeability in magma and lava. *Earth and Planetary Science Letters*, *433*, 116–124. https://doi.org/10.1016/j.epsl.2015.10.031

Klinkenberg, L. J. (1941). The permeability of porous media to liquids and gases, *Drilling and production practice* (pp. 200–213). New York: American Petroleum Institute. Retrieved from https://www.onepetro.org/conference-paper/API-41-200

Klug, C., & Cashman, K. (1994). Vesiculation of May 18, 1980, Mount St. Helens magma. *Geology*, *22*, 468–472. https://doi.org/10.1130/0091-7613(1994)022<0468:VOMMSH>2.3.CO;2

Klug, C., & Cashman, K. (1996). Permeability development in vesiculating magmas: Implications for fragmentation. *Bulletin of Volcanology*, *58*, 87–100. https://doi.org/10.1007/s004450050128

Klug, C., Cashman, K. V., & Bacon, C. R. (2002). Structure and physical characteristics of pumice from the climactic eruption of Mount Mazama (Crater Lake), Oregon. *Bulletin of Volcanology*, *64*, 486–501. https://doi.org/10.1007/s00445-002-0230-5

Kozono, T., & Koyaguchi, T. (2009a). Effects of relative motion between gas and liquid on 1-dimensional steady flow in silicic volcanic conduits: 1. An analytical method. *Journal of Volcanology and Geothermal Research*, *180*, 21–36. https://doi.org/10.1016/j.jvolgeores.2008.11.006

Kozono, T., & Koyaguchi, T. (2009b). Effects of relative motion between gas and liquid on 1-dimensional steady flow in silicic volcanic conduits: 2. Origin of diversity of eruption styles. *Journal of Volcanology and Geothermal Research*, *180*, 37–49. https://doi.org/10.1016/j.jvolgeores.2008.11.007

Kushnir, A. R. L., Martel, C., Champallier, R., & Arbaret, L. (2017). In situ confirmation of permeability development in shearing bubble-bearing melts and implications for volcanic outgassing. *Earth and Planetary Science Letters*, *458*, 315–326. https://doi.org/10.1016/j.epsl.2016.10.053

Lara, L. E. (2009). The 2008 eruption of the Chaitén Volcano, Chile: A preliminary report. *Andean Geology*, *36*, 125–129.

Lasseux, D., & Valdés-Parada, F. J. (2017). On the developments of Darcy's law to include inertial and slip effects. *Comptes Rendus Mecanique*, *345*, 660–669. https://doi.org/10.1016/j.crme.2017.06.005

Lindoo, A., Larsen, J. F., Cashman, K. V., Dunn, A. L., & Neill, O. K. (2016). An experimental study of permeability development as a function of crystal-free melt viscosity. *Earth and Planetary Science Letters*, *435*, 45–54. https://doi.org/10.1016/j.epsl.2015.11.035

Liu, Y., Zhang, Y., & Behrens, H. (2005). Solubility of H_2O in rhyolitic melts at low pressures and a new empirical model for mixed H_2O–CO_2 solubility in rhyolitic melts. *Journal of Volcanology and Geothermal Research*, *143*, 219–235. https://doi.org/10.1016/j.jvolgeores.2004.09.019

Martel, C., & Iacono-Marziano, G. (2015). Timescales of bubble coalescence, outgassing, and foam collapse in decompressed rhyolitic melts. *Earth and Planetary Science Letters*, *412*, 173–185. https://doi.org/10.1016/j.epsl.2014.12.010

Mastin, L. G. (2005). The controlling effect of viscous dissipation on magma flow in silicic conduits. *Journal of Volcanology and Geothermal Research*, *143*, 17–28. https://doi.org/10.1016/j.jvolgeores.2004.09.008

McKenzie, D. (1984). The generation and compaction of partially molten rock. *Journal of Petrology*, *25*, 713–765.

Mecke, K. R., & Seyfried, A. (2002). Strong dependence of percolation thresholds on polydispersity. *Europhysics Letters*, *58*, 28–34. https://doi.org/10.1209/epl/i2002-00601-y

Melnik, O., Barmin, A. A., & Sparks, R. S. J. (2005). Dynamics of magma flow inside volcanic conduits with bubble overpressure buildup and gas loss through permeable magma. *Journal of Volcanology and Geothermal Research*, *143*, 53–68. https://doi.org/10.1016/j.jvolgeores.2004.09.010

Melnik, O., & Sparks, R. S. J. (1999). Nonlinear dynamics of lava dome extrusion. *Nature*, *402*, 37–41. https://doi.org/10.1038/46950

Melnik, O., & Sparks, R. S. J. (2002). Dynamics of magma ascent and lava extrusion at Soufriere Hills Volcano, Montserrat. In T. H. Druitt & B. P. Kokelaar (Eds.), *The eruption of Soufriere Hills Volcano, Montserrat, from 1995 to 1999* (Vol. 21, pp. 153–171). London: Geological Society Memoirs.

Michaut, C., Bercovici, D., & Sparks, R. S. J. (2009). Ascent and compaction of gas rich magma and the effects of hysteretic permeability. *Earth and Planetary Science Letters*, *282*, 258–267. https://doi.org/10.1016/j.epsl.2009.03.026

Mueller, S., Scheu, B., Kuepper, U., Spieler, O., Richard, D., & Dingwell, B. B. (2011). The porosity of pyroclasts as an indicator of volcanic explosivity. *Journal of Volcanology and Geothermal Research*, *203*, 168–174. https://doi.org/10.1016/j.jvolgeores.2011.04.006

Nairn, I. A., Shane, P. R., Cole, J. W., & Leonard, G. J. (2004). Rhyolite magma processes of the ∼ AD 1315 Kaharoa eruption episode, Tarawera volcano, New Zealand. *Journal of Volcanology and Geothermal Research*, *131*, 265–294. https://doi.org/10.1016/S0377-0273(03)00381-0

Namiki, A. (2012). An empirical scaling of shear-induced outgassing during magma ascent: Intermittent magma ascent causes effective outgassing. *Earth and Planetary Science Letters*, *353–354*, 72–81. https://doi.org/10.1016/j.epsl.2012.08.007

Namiki, A., & Manga, M. (2008). Transition between fragmentation and permeable outgassing of low viscosity magmas. *Journal of Volcanology and Geothermal Research*, *169*, 48–60. https://doi.org/10.1016/j.jvolgeores.2007.07.020

Newman, S., Epstein, S., & Stolper, E. M. (1988). Water, carbon dioxide, and hydrogen isotopes in glasses from the ca. 1340 A.D. eruption of the Mono Craters, California: Constraints on degassing phenomena and initial volatile content. *Journal of Volcanology and Geothermal Research*, *35*, 75–96. https://doi.org/10.1016/0377-0273(88)90007-8

Nguyen, C. T., Gonnermann, H. M., Chen, Y., Huber, C., Maiorano, A. A., Gouldstone, A., & Dufek, J. (2013). Film drainage and the lifetime of bubbles. *Geochemistry, Geophysics, Geosystems*, *14*, 3616–3631. https://doi.org/10.1002/ggge.20198

Nguyen, C. T., Gonnermann, H. M., & Houghton, B. F. (2014). Explosive to effusive transition during the largest volcanic eruption of the 20th century (Novarupta 1912, Alaska). *Geology*, *42*, 703–706. https://doi.org/doi: 10.1130/G35593.1

Okumura, S., Nakamura, M., Takeuchi, S., Tsuchiyama, A., Nakano, T., & Uesugi, K. (2009). Magma deformation may induce non-explosive volcanism via degassing through bubble networks. *Earth and Planetary Science Letters*, *281*, 267–274. https://doi.org/10.1016/j.epsl.2009.02.036

Ollion, J., Cochennec, J., Loll, F., Escudé, C., & Boudier, T. (2013). TANGO: A generic tool for high-throughput 3D image analysis for studying nuclear organization. *Bioinformatics*, 1840–1841. https://doi.org/10.1093/bioinformatics/btt276

Papale, P. (1999). Strain-induced magma fragmentation in explosive eruptions. *Nature*, *397*, 425–428. https://doi.org/10.1038/17109

Polacci, M., & Papale, P. (2001). Textural heterogeneities in pumices from the climactic eruption of Mount Pinatubo, 15 June 1991, and implications for magma ascent dynamics. *Bulletin of Volcanology*, *63*, 83–97. https://doi.org/10.l007/s004450000123

Proussevitch, A. A., Sahagian, D. L., & Kutolin, V. A. (1993). Stability of foams in silicate melts. *Journal of Volcanology and Geothermal Research*, *59*, 161–178. https://doi.org/10.1016/0377-0273(93)90084-5

Rust, A. C., & Cashman, K. V. (2004). Permeability of vesicular silicic magma: Inertial and hysteresis effects. *Earth and Planetary Science Letters*, *228*, 93–107. https://doi.org/10.1016/j.epsl.2004.09.025

Rust, A. C., & Cashman, K. V. (2011). Permeability controls on expansion and size distributions of pyroclasts. *Journal of Geophysical Research*, *116*, B11202. https://doi.org/10.1029/2011JB008494

Saar, M., & Manga, M. (1999). Permeability - porosity relationship in vesicular basalts. *Geophysical Research Letters*, *26*, 111–114. https://doi.org/10.1029/1998GL900256

Saubin, E., Tuffen, H., Gurioli, L., Owen, J., Castro, J. M., Berlo, K., . . . Wehbe, K. (2016). Conduit dynamics in transitional rhyolitic activity recorded by tuffisite vein textures from the 2008–2009 Chaitén eruption. *Frontiers of Earth Sciences*, *4*, 2095–17. https://doi.org/10.3389/feart.2016.00059

Schindelin, J., Arganda-Carreras, I., Frise, E., Kaynig, V., Longair, M., Pietzsch, T., . . . Cardona, A. (2012). Fiji: An open-source platform for biological-image analysis. *Nature Methods*, *9*, 676–682. https://doi.org/10.1038/nmeth.2019

Schipper, C. I., Castro, J. M., Tuffen, H., James, M. R., & How, P. (2013). Shallow vent architecture during hybrid explosive–effusive activity at Cordón Caulle (Chile, 2011–12): Evidence from direct observations and pyroclast textures. *Journal of Volcanology and Geothermal Research*, *262*, 25–37. https://doi.org/10.1016/j.jvolgeores.2013.06.005

Self, S., Kircher, D. E., & Wolff, J. E. (1988). The El Cajete series, Valles Caldera, New Mexico. *Journal of Geophysical Research*, *93*, 6113–6127. https://doi.org/10.1029/JB093iB06p06113

Seligman, A. N., Bindeman, I. N., Watkins, J. M., & Ross, A. M. (2016). Water in volcanic glass: From volcanic degassing to secondary hydration. *Geochimica et Cosmochimica Acta*, *191*, 216–238. https://doi.org/10.1016/j.gca.2016.07.010

Shea, T., Gurioli, L., & Houghton, B. F. (2012). Transitions between fall phases and pyroclastic density currents during the AD 79 eruption at Vesuvius: Building a transient conduit model from the textural and volatile record. *Bulletin of Volcanology*, *74*, 2363–2381. https://doi.org/10.1007/s00445-012-0668-z

Shea, T., Hellebrand, E., Gurioli, L., & Tuffen, H. (2014). Conduit- to localized-scale degassing during Plinian eruptions: Insights from major element and volatile (Cl and H_2O) analyses within Vesuvius AD 79 pumice. *Journal of Petrology*, *55*, 315–344. https://doi.org/10.1093/petrology/egt069

Shea, T., Houghton, B. F., Gurioli, L., Cashman, K. V., Hammer, J. E., & Hobden, B. J. (2010). Textural studies of vesicles in volcanic rocks: An integrated methodology. *Journal of Volcanology and Geothermal Research*, *190*, 271–289. https://doi.org/10.1016/j.jvolgeores.2009.12.003

Sparks, R. S. J. (1978). The dynamics of bubble formation and growth in magmas: A review and analysis. *Journal of Volcanology and Geothermal Research*, *3*, 1–37. https://doi.org/10.1016/0377-0273(78)90002-1

Sparks, S. J., Barclay, J., Jaupart, C., Mader, H. M., & Phillips, J. C. (1994). Physical aspects of magmatic degassing I. experimental and theoretical constraints on magma vesiculation. In M. R. Carroll & J. R. Holloway (Eds.), *Volatiles in magmas, Reviews in Mineralogy* (Vol. 30, pp. 413–446). Washington, DC: Mineralogical Society of America.

Stasiuk, M. V., Barclay, J., Carroll, M. R., Jaupart, C., Ratté, J. C., Sparks, R. S. J., & Tait, S. R. (1996). Degassing during magma ascent in the Mule Creek vent (USA). *Bulletin of Volcanology*, *58*, 117–130. https://doi.org/10.1007/s004450050130

Stauffer, D., & Aharony, A. (1994). *Introduction to percolation theory* (2nd edn., p. 192). Boca Raton, FL, USA: CRC Press.

Stevenson, R. J., Dingwell, D. B., Webb, S. L., & Sharp, T. G. (1996). Viscosity of microlite-bearing rhyolitic obsidians: An experimental study. *Bulletin of Volcanology*, *58*, 298–309.

Swanson, S. E., Naney, M. T., Westrich, H. R., & Eichelberger, J. C. (1989). Crystallization history of Obsidian Dome, Inyo Domes, California. *Bulletin of Volcanology*, *51*, 161–176. https://doi.org/10.1007/BF01067953

Takeuchi, S., Nakashima, S., & Tomiya, A. (2008). Permeability measurements of natural and experimental volcanic materials with a simple permeameter: Toward an understanding of magmatic degassing processes. *Journal of Volcanology and Geothermal Research*, *177*, 329–339. https://doi.org/10.1016/j.jvolgeores.2008.05.010

Takeuchi, S., Tomiya, A., & Shinohara, H. (2009). Degassing conditions for permeable silicic magmas: Implications from decompression experiments with constant rates. *Earth and Planetary Science Letters*, *283*, 101–110. https://doi.org/10.1016/j.epsl.2009.04.001

Taylor, B., Eichelberger, J., & Westrich, H. (1983). Hydrogen isotopic evidence of rhyolitic magma degassing during shallow intrusion and eruption. *Nature*, *306*, 541–545.

Thomas, N., Jaupart, C., & Vergniolle, S. (1994). On the vesicularity of pumice. *Journal of Geophysical Research*, *99*, 15,633–15,644. https://doi.org/10.1029/94JB00650

Toramaru, A. (1988). Formation of propagation pattern in two-phase flow systems with application to volcanic eruptions. *Geophysical Journal*, *95*, 613–623. https://doi.org/10.1111/j.1365-246X.1988.tb06707.x

Toramaru, A. (1990). Measurement of bubble size distribution in vesiculated rocks with implications for quantitative estimation of eruption processes. *Journal of Volcanology and Geothermal Research*, *43*, 71–90. https://doi.org/10.1016/0377-0273(90)90045-H

Tuffen, H., Dingwell, D. B., & Pinkerton, H. (2003). Repeated fracture and healing of silicic magma generate flow banding and earthquakes? *Geology*, *31*, 1089–1092. https://doi.org/10.1130/G19777.1

Tuffen, H., Smith, R., & Sammonds, P. R. (2008). Evidence for seismogenic fracture of silicic magma. *Nature*, *453*, 511–514. https://doi.org/10.1038/nature06989

Wallace, P. J. (2005). Volatiles in subduction zone magmas: Concentrations and fluxes based on melt inclusion and volcanic gas data. *Journal of Volcanology and Geothermal Research*, *140*, 217–240. https://doi.org/10.1016/j.jvolgeores. 2004.07.023

Webb, S. L., & Dingwell, D. B. (1990). Non-Newtonian rheolgy of igneous melts at high stresses and strain rates: Experimental results for rhyolite, andesite, basalt, and nephelinite. *Journal of Geophysical Research*, *95*, 15,695–15,701. https://doi.org/10.1029/JB095iB10p15695

Westrich, H. R., & Eichelberger, J. C. (1994). Gas transport and bubble collapse in rhyolitic magma: An experimental approach. *Bulletin of Volcanology*, *56*, 447–458. https://doi.org/10.1007/BF00302826

Wilson, C. J. N., & Hildreth, W. (1997). The Bishop Tuff: New insights from eruptive stratigraphy. *Journal of Geology*, *105*, 407–440. https://doi.org/10.1086/515937

Wolff, J. A., Brunstad, K. A., & Gardner, J. N. (2011). Reconstruction of the most recent volcanic eruptions from the Valles caldera, New Mexico. *Journal of Volcanology and Geothermal Research*, *199*, 53–68. https://doi.org/10.1016/j.jvolgeores.2010.10.008

Woods, A. W., & Koyaguchi, T. (1994). Transitions between explosive and effusive eruptions of silicic magmas. *Nature*, 641–644. https://doi.org/10.1086/515937

Xu, W., Su, X., & Jiao, Y. (2016). Continuum percolation of congruent overlapping spherocylinders. *Physical Review E: Covering Statistical, Nonlinear, Biological, and Soft Matter Physics*, *94*(32), 122–8. https://doi.org/10.1103/PhysRevE.94.032122

Yi, Y. B., & Sastry, A. M. (2004). Analytical approximation of the percolation threshold for overlapping ellipsoids of revolution. *Proceedings of the Royal Society A: Mathematical, Physical and Engineering Sciences*, *460*, 2353–2380. https://doi.org/10.1098/rspa.2004.1279